SUBMESOSCALE DYNAMICS AND TRANSPORT PROPERTIES IN THE GULF OF MEXICO

A Thesis
Presented to
The Academic Faculty

by

Yisen Zhong

In Partial Fulfillment
of the Requirements for the Degree
Doctor of Philosophy in the
School of Earth and Atmospheric Sciences

Georgia Institute of Technology
December, 2013

SUBMESOSCALE DYNAMICS AND TRANSPORT PROPERTIES IN THE GULF OF MEXICO

Approved by:

Dr. Annalisa Bracco, Advisor
School of Earth and Atmospheric Sciences
Georgia Institute of Technology

Dr. Emanuele Di Lorenzo
School of Earth and Atmospheric Sciences
Georgia Institute of Technology

Dr. Robert X. Black
School of Earth and Atmospheric Sciences
Georgia Institute of Technology

Dr. Tracy A. Villareal
Marine Science Institute
The University of Texas at Austin

Dr. Takamitsu Ito
School of Earth and Atmospheric Sciences
Georgia Institute of Technology

Date Approved: November 12, 2013

ACKNOWLEDGEMENTS

First and foremost, I would like to express my deepest gratitude to my advisor Prof. Annalisa Bracco, who has provided me invaluable guidance and continuous support for the past five years. This thesis would not have been possible without her.

I would also like to thank my thesis reviewers: Prof. Tracy A. Villareal, Prof. Taka Ito, Prof. Emanuele Di Lorenzo, and Prof. Robert X. Black. Their insightful comments and suggestions helped improve the quality of this thesis.

I am very grateful to my group members for their warm assistance on my research, and to my friends for their making my graduate life enjoyable.

Finally I want to thank my parents and my love. They have been always encouraging me and supporting me with their best wishes.

TABLE OF CONTENTS

Page

ACKNOWLEDGEMENTS iii

LIST OF FIGURES v

SUMMARY viii

CHAPTER

1 INTRODUCTION 1

2 SUBMESOSCALE IMPACT ON THE SURFACE TRACER DISTRIBUTION#

2.1 Introduction 5

2.2 Model and Configuration 10

2.3 Results 14

2.4 Conclusion and Discussion 32

3 SUBMESOSCALE IMPACT ON HORIZONTAL AND VERTICAL TRANSPORT 35

3.1 Introduction 36

3.2 Model and Configuration 38

3.3 The Eulerian Flow 42

3.4 The Lagrangian Trajectory 59

3.5 Horizontal and Vertical Lagrangian Transport 65

3.6 Conclusion and Discussion 75

4 CONCLUSIONS AND FUTURE WORKS 78

4.1 Conclusion 78

4.2 Future works 81

REFERENCES 83

LIST OF FIGURES

Page

Figure 2.1: Ocean color satellite images of *Sargassum*. (A): *Sargassum* lines in a MERIS MCI (Maximum Chlorophyll Index) image on June 2, 2005. (B): A patch observed by the same satellite in the North Atlantic on September 4, 2008. The center of the patch is located at 35°45'N and 66°21'W and its diameter is approximately 45 km. …… 7

Figure 2.2: Relative vorticity scaled by the Coriolis parameter (ζ/f) at the surface (1 m, Panel A) and at 106 m (Panel B) in the idealized integration 60 days after particle deployment, and (Panel C and D) the corresponding particle distribution. Axes are in km. ……. 16

Figure 2.3: Distribution of Lagrangian particles deployed at 1 m depth after two days (Panel A), after two weeks (Panel B) and after 60 days (Panel C), with zooms on distributions of particles deployed inside one vortex overlying the horizontal divergence field (in color). The vortex is destroyed during a merging event after 40 days. Units of divergence field are $10^{-5}s^{-1}$. …….. 21

Figure 2.4: Probability of surface particles of falling into areas with different divergence values (aka PDF) at different time during the integration. The x-axis is divergence. (Unit: $10^{-5}s^{-1}$). …… 22

Figure 2.5: Same as in Figure 2.3 but for particles and divergence field at 106 m depth. The divergence field is plotted using the same color scale in Figure 2.3. …… 23

Figure 2.6: Same as in Figure 2.4 but for particles at 106 m depth. …….. 24

Figure 2.7: A snapshot of surface relative vorticity scaled by the Coriolis parameter (ζ/f) in the western Gulf of Mexico in May. The four regions described in the text are marked *A* to *D*. …… 27

Figure 2.8: Distribution of surface Lagrangian particles overlying the horizontal divergence field (in color, Unit: $10^{-5}s^{-1}$) in the western Gulf of Mexico on May 1, 2005, with zooms on Region *A* and *B*. …….. 28

Figure 2.9: Probability of surface particles of falling into areas with different divergence values in the western Gulf of Mexico on May 1, 2005. The x-axis is divergence. (Unit: $10^{-5}s^{-1}$). ……. 29

Figure 2.10: (A): Relative vorticity scaled by Coriolis parameter and (B): divergence field at 100 m depth in the Gulf of Mexico. (The unit for the divergence is 10^{-5} s^{-1}). ……. 30

Figure 2.11: Distribution of surface Lagrangian particles in the western Gulf of Mexico on February 26, 2005, with a zoom over the large Loop Eddy overlying the horizontal divergence field (in color; Unit: $10^{-5}s^{-1}$). The horizontal resolution of this run is 2 km. …….. 31

Figure 3.1: Snapshots of surface relative vorticity (top panels) and surface horizontal shear (bottom panels), scaled by the Coriolis parameter *f* on April 21, 2005. (a) and (c) 1 km nested run. (b) and (d) 5 km parent grid. The black boxes indicate where Lagrangian particles are deployed. ……. 42

Figure 3.2: Time series of daily averaged eddy kinetic energy during the Lagrangian deployment period in the parent (red) and nested (blue) grids. The correlation coefficient between the two curves is cc = 0.98. …… 43

Figure 3.3: Azimuthally-integrated spatial power spectra of surface horizontal kinetic energy at the three deployment depths for the 1 km (in blue) and the 5 km (in red) resolution runs. (Unit: m^3/s^2). ……... 45

Figure 3.4: Panel (a): Probability density function (PDF) of Eulerian horizontal velocities at 50 m, normalized to have unit variance. Panel (b): PDF of relative vorticity at the surface and 100 m depth, normalized to have unit variance. …… 47

Figure 3.5: Transects of temperature along 94.3°W (where the Lagrangian particles are released) averaged over April 21–May 4, 2005, and zoom of the top 700 m of the water column. (a) 1 km and (b) 5 km resolution runs. ……. 48

Figure 3.6: Instantaneous (a and b) and 7-day averaged (c and d) vertical velocity at 5 m depth. (a) and (c): 1 km resolution run; (b) and (d): 5 km resolution run. (Unit: m/day). ……. 50

Figure 3.7: Same as in Figure 3.6 but for 100 m depth. …… 51

Figure 3.8: Instantaneous pattern of $\left|\nabla_h \rho\right|$ at 5 m (top panels) and 100 m (middle panels) of 1 km (a and c) and 5 km (b and d) runs on April 21, 2005 (Unit: 10^{-5} kg m^{-4}), and their azimuthally-integrated power spectra (e). ……. 53

Figure 3.9: Panel (a): Domain-averaged vertical profile of the root-mean-square fluctuation of instantaneous vertical velocities (solid lines) and of their low-pass filtered counterpart with the cut-off frequency 0.8*f* (Unit: m/day). Panel (b): frequency power spectra of vertical velocities at 5, 50, 100 and 1000 m. (Unit: m^2/s^2 h). In both figures only regions where the water column is deeper than 750 m have been considered. …… 55

Figure 3.10: Probability density function of Eulerian vertical velocities at 50 m, normalized to have unit variance, compared to a Gaussian distribution. ….. 56

Figure 3.11: Distribution of isobaric (2-D) particles superposed on the relative vorticity field normalized by the Coriolis frequency *f* at 5 m (top panels) and 100 m (bottom panels) 40 days after deployment. (a-c) 1 km resolution and (b-d) 5 km resolution integrations. …… 61

Figure 3.12: Vertical distribution of 3-D particles 40 days after deployment. The color of the particles indicates their depth (Unit: m). (a) and (b): Tracers initially released at 5 m in the 1 km and 5 km horizontal resolution runs, respectively. (c) and (d): Tracers initially released at 100 m in the 1 km and 5 km resolution integrations. …….. 63

Figure 3.13: Probability density function (PDF) of the vertical displacement of 3-D particles 10, 20, 30, and 40 days after deployment in the nested (blue curves) and parent (red curves) simulations. (a): PDF for particles deployed at 5 m; (b): PDF for particles deployed at 100 m. ……. 64

Figure 3.14: Horizontal absolute dispersion of 3-D particles initially released at (a) 5 m, (b) 50 m, and (c) 100 m depth. In (a) and (c) dispersion curves of isobaric (2-D) particles are also plotted. ……... 69

Figure 3.15: Finite size Lyaponov exponents of 2-D particles at 5 m and 100 m depths in the nested (blue curves) and parent (red curves) simulations. Particles are deployed at a minimum distance of 1 km in both runs. The gray portions of the red curves indicate displacements below the model grid scale. …….. 71

Figure 3.16: Vertical absolute dispersion of 3-D particles initially released at (a) 5 m, (b) 50 m, and (c) 100 m depth. …….. 74

SUMMARY

Submesoscale processes, characterized by O(1km) horizontal scale and O(1) Rossby number, are ubiquitous in the world ocean and play an important role in the vertical flux of mass, buoyancy and tracers in the upper ocean. However, they have not been intensively studied due to the requirement of uniquely high spatial and temporal resolution in the observation and computer modeling. In this thesis, using a suite of high-resolution numerical experiments in the northwestern Gulf of Mexico, where rich submesoscale structures are accompanied by the strong mesoscale Loop Current eddies, the impact of resolving submesoscales on the tracer distribution and 3-D transport was extensively examined. It was concluded that, submesoscale dynamics aggregated the surface tracers and formed characteristic patterns at scales of kilometers near the ocean surface by enhanced convergence/divergence zones associated with strong ageostrophic processes. This distinctive phenomenon was evident in recent ocean color satellite images which showed similar extensive lines and spirals of floating *Sargassum* in the western Gulf of Mexico. In addition, better-resolved submesoscale activities increased the horizontal resolution dramatically and elevated local vertical velocity both within and below the mixed layer while leaving the horizontal component almost unaltered. The vertical dispersion increased by several fold with the largest difference close to the surface. Considering the pervasive presence of submesoscale structures at the surface ocean, these models predict that submesoscale processes may serve as an important nutrient supply mechanism in the upper ocean and potentially make a significant contribution on balancing the global biogeochemical tracer budget.

CHAPTER 1

INTRODUCTION

The processes at scales of O(1km) with O(1) Rossby number, termed as submesoscale processes, have recently attracted increasing attention due to the characteristic dynamic structures such as fronts, filaments etc. and their ubiquitousness in the upper ocean (Mahadevan and Tandon, 2006; Capet et al., 2008a, 2008b, 2008c; Thomas et al., 2008; Gildor et al., 2009; Klein and Lapeyre, 2009; Zhong et al., 2012). Unlike mesoscale dynamics, submesoscale dynamics cannot be properly described by the traditional quasi-geostrophic (QG) approximation due to the development of secondary ageostrophic circulation (McWilliams, 1989; Smith and Vallis, 2001), and they are also not fully three-dimensional (3-D) or non-hydrostatic either (Madahevan et al., 2006). However, submesoscale processes provide a pathway for energy transference between the meso- and dissipation scales, and their unique dynamic characteristics play a critical role in the vertical exchange of mass, tracers and buoyancy in the upper ocean.

In the ocean, the mesoscale eddies and large scale circulations are the most dominant and energetic dynamic phenomena and store a large portion of kinetic energy. However, they are approximately in a force-balance state (hydrostatic and geostrophic balance) and therefore it is difficult to convert the available potential energy to kinetic energy (KE) and transfer KE from the mesoscale to the dissipation scale where the energy dissipation occurs. Recent numerical studies have showed a faster energy transferring rate in the submesoscale range by identifying a horizontal kinetic energy wavenumber spectrum flatter than k^{-3} contrary to the prevailing view of mesoscale

dynamics, which implies that the submesoscale processes and associated ageostrophic instability can break down the balanced state and promote forward KE cascade (Capet et al., 2008c, Zhong and Bracco, 2013).

The submesoscale processes are particularly dominant in the upper ocean and largely impact the surface tracer dispersion and its vertical flux. Submesoscale structures such as eddies, fronts, and filaments at the ocean surface, can create complex patterns of tracers in the distribution of temperature, salinity, nutrient and phytoplankton (Levy, 2012; Zhong et al, 2012; Zhong and Bracco, 2013). The large vertical velocity associated with the ageostrophic motion is not only of much interest in physics but also critical to biological processes and air-sea exchanges. Previous studies have shown that vertical nutrient supply due to mesoscale eddies represents a significant portion in the global nutrient requirement but seems still insufficient to balance the new production in geochemical estimates (McGillicuddy et al., 2003, 2007). It is suggested that the ageostrophic secondary circulation associated with the submesoscale processes can induce vertical velocity on the order of 10-100 m/day along the periphery of the eddies and therefore makes a major contribution to the nutrient replenishment in the upper ocean (Mahadevan et al., 2008).

Although the potential importance of submesoscale has been well recognized, there are still many unknown issues related to submesoscale dispersion, transport and mixing etc. In this thesis, two questions will be focused on and addressed using a suite of high-resolution numerical simulation. Chapter 2 will investigate how ocean submesoscales regulate the surface tracer distribution. The numerical results are compared well with the distribution of the floating *Sargassum* observed in the satellite images. The impact of the

submesoscale processes on the ocean transport, particularly its vertical component, will be discussed in the Chapter 3. The study area is selected as the Gulf of Mexico, where the stirring of the energetic mesoscale eddies (Loop Current Eddies) generates a large amount of submesoscale structures. The result will also be instrumental in studying recent disastrous BP oil spill event. Including submesoscale dynamics helps predict the oil trajectories more accurately.

CHAPTER 2

SUBMESOSCALE IMPACT ON THE SURFACE TRACER DISTRIBUTION

Published as:

Zhong, Y., A. Bracco and T. A. Villareal. Pattern formation at the ocean surface: *Sargassum* distribution and the role of the eddy field. *Limnol. Oceanogr.* 2:12-27, 2012

Abstract

Positively buoyant organisms such as the macroalgae *Sargassum* and the cyanobacterium *Trichodesmium* often form surface accumulations visible in satellite imagery that have lateral scale separation of tens of kilometers and cannot be explained by Langmuir circulation. Here we discuss the accumulation of floating materials in the ocean in presence of meso- and submesoscale activity. Using high resolution simulations of the ocean mesoscale in both idealized (a 3-D box where coherent eddies are forced by small-scale winds) and realistic domains (western Gulf of Mexico), where extensive concentrations of floating *Sargassum* have been recorded in satellite images, we show that the distribution of tracers at ocean surface departs rapidly from the one observed few tens of meters below it. Such distribution does not resemble that observed for passive tracers in quasi-geostrophic turbulence.

The strong divergence and convergence zones generated at the surface by ageostrophic processes in the submesoscale range are responsible for the creation of areas where the floating material accumulates. Floating particles are expelled from the core of mesoscale eddies, and concentrate in convergence regions in patterns comparable to the ones observed through the satellite images. In light of those results, *Sargassum* and/or *Trichodesmium* may provide a useful proxy to track convergence/divergence processes resulting from ageostrophic processes at the ocean surface.

2.1 Introduction

In the ocean, Lagrangian observations in the form of drifter or float trajectories are often used to study the surface dynamics such as dispersion and transport properties (see review LaCasce, 2008 for example). As such, natural biological tracers can also help in the understanding of the physical processes at play and to this end the distribution of free-floating *Sargassum* (Phaeophyceae) has captured the interest of physical oceanographers and marine biologists for decades. *Sargassum* is a highly visible macrophytic algae widely distributed in the North Atlantic, Caribbean, and Gulf of Mexico that provides a crucial habitat for a myriad of marine organisms (Butler et al., 1983; Rooker et al., 2004). In 1923, Winge first reported that *Sargassum* algae always align themselves with local wind direction to form an irregular pattern of fractional parallel lines (aka windrows). Those streaks may extend to a few hundred meters in length with typical separations between wind-wave lines of 20 m to 50 m comparable to the boundary-layer depth (Faller and Woodcock, 1964). Langmuir systematically investigated the lines of *Sargassum* through a series of experiments on Lake George and concluded that they were, in fact,

dictated by a quasi-steady circulation, afterwards named Langmuir circulation (Langmuir, 1938).

More recently, extensive 'lines' of *Sargassum* of much larger magnitude have been detected in ocean color satellite images of Gulf of Mexico and the West Atlantic Ocean (Gower et al., 2006; Gower and King, 2008). The Gulf of Mexico, together with the Sargasso Sea, has the largest concentration of floating *Sargassum* biomass in the world (Gower and King, 2011). The satellite observations were the first to map the patchiness of the *Sargassum* at the ocean mesoscales, and note widespread lines, typically 10-100 kilometers long and kilometers wide (Figure 2.1). The range of scales involved suggests that physical structures like eddies, filaments and fronts are likely responsible for this phenomenon and may control the dispersion and aggregation of *Sargassum*, as well as other floating material, at the ocean surface. Similar patterns are also evident in reflectance images of the oceanic surface and have been linked to the ageostrophic intensification of cold filaments by the horizontal shear associated with mesoscale eddies (McWilliams et al., 2009a).

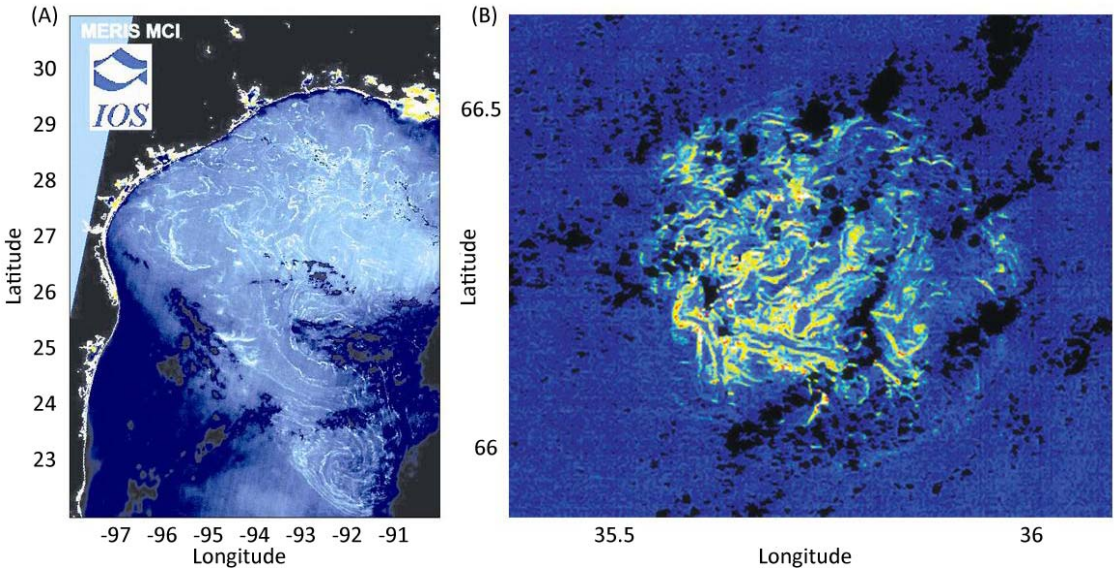

Figure 2.1: Ocean color satellite images of *Sargassum*. (A): *Sargassum* lines in a MERIS MCI (Maximum Chlorophyll Index) image on June 2, 2005 (http://www.esa.int/esaCP/SEMHO6ARR1F_index_1.html#subhead1, also in Gower et al. 2006). (B): A patch observed by the same satellite in the North Atlantic on September 4, 2008 (http://www.esa.int/esaEO/SEMH61AWYNF_index_2.html). The center of the patch is located at 35°45'N and 66°21'W and its diameter is approximately 45 km (Credit: ESA).

In the ocean, coherent vortices or eddies form spontaneously by baroclinic or barotropic instability under the influence of rapid rotation and stable stratification or by interaction of the main currents with topographic features. These vortices/eddies move in a chaotic manner while embedded in a background turbulence field. Here 'coherent' refers to the vortices' lifetime, which is much longer than their turnover time. In the last three decades, the transport and mixing properties associated with coherent vortices have been studied in detail in the context of two-dimensional (2-D) (McWilliams, 1990; Elhmaidi et al., 1993; Provenzale, 1999) and quasi-geostrophic (QG) (Smith and Vallis,

2001; Bracco et al., 2004) turbulence flows in both Eulerian and Lagrangian frameworks. Coherent vortices are impermeable to inward and outward fluxes and can retain their physical and chemical properties over their lifetime. They have been described as "islands of regular Lagrangian dynamics in a chaotic background" (Provenzale, 1999) and different dispersion behaviors have been identified depending on where Lagrangian tracers reside – inside, outside or within the circulation cells around the eddies. According to 2-D and QG theories, however, the distribution of tracers (i.e., temperature, salinity, chemical or biological concentrations) is uniform within each topological region (vortices, circulation cells or background turbulence) and no aggregation or accumulation can take place. In other words, the mesoscale vortices represent the only level of patchiness present in the Eulerian flow, while the distributions of Lagrangian tracers remain homogeneous. In agreement with those findings, in the ocean it has been observed that coherent eddies can maintain the characteristics of their source waters for several months and over hundreds of kilometers (Richardson, 1993; McDonagh and Heywood, 1999). They can trap floats (Richardson, 1993; Paillet, 1999; Shoosmith et al., 2005), and they are responsible for anomalous dispersion curves (Rupolo et al., 1996; Berloff et al., 2002; Reynolds, 2002), Lagrangian power spectra (Rupolo et al., 1996) and horizontal velocity distributions (Bracco et al., 2000; Bracco et al., 2003) in agreement with 2-D and QG turbulence predictions. Those properties, all assessed below the ocean surface, have been confirmed in a recent study using a regional ocean model at 1 km horizontal resolution with an idealized configuration mimicking a baroclinic wind-induced vortex system (Koszalka et al., 2009). The same study, however, pointed out that the motion at the submesoscale (~ 1 km scale) within and immediately around eddies is strongly

ageostrophic, in contradiction with the geostrophically balanced 2-D or QG approximations. This result contributed to the view of a surface ocean dominated by strong and complex vorticity patterns generated by ageostrophic processes, already established for frontal systems (Capet et al., 2008a,b; Thomas et al., 2008).

Fronts, i.e., narrow regions of very large lateral buoyancy gradients, are also ubiquitous in the upper ocean (Ullman and Cornillon, 1999; Capet et al., 2008b). Fronts are characterized by strong lateral velocity shear and relative vorticity of the opposite sign on either side. Strong frontogenesis can occur also around the edge of the mesoscale eddies due to the high strain rate between the rapidly spinning eddy and background flow. The large vorticity gradients at front edges suggest that frontal motion is characterized by a loss of geostrophic balance (Capet et al., 2008a,b,c). It has been shown recently that frontal instability acting at the submesoscales plays a crucial role in transferring energy down to the dissipation scale (McWilliams et al., 2003; Molemaker et al., 2005; Capet et al., 2008c). Additionally, large vertical velocities (substantially larger than mesoscale counterpart) develop inside the fronts (Thomas and Ferrari, 2008), and they are instrumental in exchanging physical, chemical and biological properties between the ocean surface and the interior (Mahadevan et al. 2008).

In this chapter, we examine how ageostrophic submesoscale processes associated with eddies and fronts determine the distribution of tracers at the ocean surface and can explain the complex patterns revealed by the satellite observations of *Sargassum*. We will present two numerical integrations: The first representing an idealized wind-driven eddy-dominated portion of the open ocean, which allows us to investigate the physical

mechanism at play, and the second covering the Gulf of Mexico, where we can compare the results to the satellite observations.

2.2 Model and Configuration

In this study, we implemented two ocean model configurations. The first configuration simulated an idealized eddy-dominated flow away from coastal boundaries, similar to that described in Koszalka et al. (2009) except for a deeper mixed layer. Its circulation was forced only by a wind field described by an analytical expression. This idealized configuration allowed us to investigate in detail the dynamical mechanism that controls the distribution of the surface particles. The second one simulated the circulation in the western Gulf of Mexico, where extensive lines of *Sargassum* have been observed using satellite measurements (Gower et al., 2006), and allowed us to validate our conclusions in a realistic domain. Both configurations include the integration of Lagrangian trajectories to mimic the behavior of passively-advected material at the ocean surface.

The Regional Ocean Modeling System (ROMS) (Shchepetkin and McWilliams, 2003; Shchepetkin and McWilliams, 2005) is a free-surface eddy-resolving primitive equation model based on the Boussinesq approximation and hydrostatic balance. It is discretized using an Arakawa C grid with orthogonal curvilinear coordinates on the horizontal and has a generalized terrain-following coordinate system (S- or sigma coordinate) with a staggered Arakama C grid in the vertical. The depth of each layer depends therefore on the local topography and sea surface height (SSH). ROMS has a split-explicit time step scheme, which implements a short time step for surface elevation

and barotropic momentum, and a longer one for baroclinic momentum and tracer variables (including temperature and salinity). Horizontal 3rd-order upstream-biased and vertical 4th-order centered difference schemes were used to advect both momentum and tracer equations. Given the high resolution of our runs, we selected horizontal biharmonic friction and diffusion to reduce small-scale noise. The vertical mixing was parameterized accordingly to the non-local K-Profile Parameterization (KPP) boundary-layer scheme (Large et al., 1994). ROMS has been successfully used to simulate the ocean circulation in regions characterized by high mesoscale activity as, for example, the California Current System (Di Lorenzo et al., 2004; Capet et al., 2008a), the Caribbean Seas (Jouanno et al., 2008) and the Labrador Sea (Luo et al., 2011).

For the idealized configuration, we adopted a periodic domain with lateral size 256 km and a constant depth of 1000 m on the *f*-plane (*f* has constant value 10^{-4} s^{-1}). The horizontal resolution of the grid was 1 km and the vertical discretization was 30 layers, 10 of which confined to the first 110 m. The depth of each layer was approximately constant because the topography is flat and the SSH variations are small compared to the total water depth. The top layer covered the first 1.93 m of the water column. An idealized wind forcing field with a narrow-band continuous spectrum centered at about 40 km with radial wave number $\sqrt{k_x^2 + k_y^2} \sim 8$ provided a close approximation to that used in previous studies to force 2-D and QG turbulence fields (Elhmaidi et al., 1993; Bracco et al., 2004). Different realizations of the wind stress field with identical power spectra were linearly interpolated every 20 days. We initialized the model from rest by imposing a vertical stratification that follows sample profiles in the extra-tropics (Conkright et al., 2002) below the top 50 m and is uniform within the surface mixed

layer. The solution was nudged to the initial vertical profile of temperature and salinity every 60 days to forestall flow barotropization and energy accumulation.

Passive Lagrangian particles were deployed in the ocean top layer at about 1 m depth as approximation of the surface, and at 106 m, once the stationary state was achieved (in the model the horizontal velocity field used to advect the Lagrangian tracers is available at the half-sigma levels). Their advection in time is described by

$$\frac{d\mathbf{x}}{dt} = \mathbf{u}(\mathbf{x}, t)$$

here **x** is the particle position vector and **u** is the corresponding Eulerian velocity vector at the particle position. The time integration of the above equation was performed on-line using a 3rd-order Milne predictor and 4th-order Hamming corrector scheme. Off-line Lagrangian diagnostics of upper ocean mixing in presence of an energized submesoscale field has been shown to lead to significant temporal sampling errors (Keating et al., 2011). No inertial effects were included and the particles moved with flow passively and did not feedback on the surrounding fluid.

ROMS includes routines for the integration of 3-D, isobaric and geopotential Lagrangian tracers. Particles move freely in the 3-D flow or are confined along the isobars and isobaths, respectively. We were interested in understanding the motion of surface floating tracers (regardless of source or sink) and a natural choice is to use isobaric particles. Model results, however, were independent on the kind of tracers adopted because at the ocean surface the vertical motion of neutrally buoyant and infinitesimally small particles is controlled uniquely by the surface boundary condition ($d\eta / dt = w$, where η is free surface elevation and w is vertical velocity). Neutrally

buoyant particles deployed at the surface will keep following the surface isobaric plane. In our simulations, we deployed the Lagrangian tracers on a uniform grid in a shallow layer with the purpose of reducing the potential numerical error at the surface. In the idealized run, 65,536 particles were integrated starting 488 days after initialization and their trajectories were followed for 60 days.

To validate the analysis of the idealized case, we also configured ROMS in the Gulf of Mexico and focused a high resolution run in the west part of the domain, where satellite images of *Sargassum* distributions are available (Gower et al., 2006). For this integration, we first spun-up the model at 5 km horizontal resolution and 30 vertical layers over the whole Gulf of Mexico. The atmospheric forcing fields were from NCEP/NCAR (National Centers for Environmental Predictions / National Center for Atmospheric Research) reanalysis (Kalnay et al., 1996) and included wind stress, surface net heat fluxes and water fluxes, and solar radiation fluxes. Climatological values over the period 1948-2001 were used. SODA (Simple Ocean Data Assimilation, Carton and Giese, 2008) reanalysis provided the nudging conditions at the open boundaries and the initial conditions. Again, monthly climatological values were employed. After ten years, the model output reached a statistically stationary state that was used as initial condition for a second experiment in which surface atmospheric forcings retain monthly variability over the period of 2002-2007. NCEP momentum fluxes were replaced by the monthly-averaged NCEP-QSCAT blended wind stresses from Colorado Research Associates (version 5.0) (Chin et al., 1998; Milliff et al., 2004). Finally, we concentrated on the western Gulf of Mexico with a nested domain at 1 km horizontal resolution. Nesting is a widely-used technique to run very high resolution simulations over limited areas,

reducing the computational costs. It embeds a child grid of finer resolution into its parent coarse grid so as to be able to resolve the details of the mesoscale and submesoscale dynamical features over the region of interest. Here we adopted an off-line one-way nesting method that has been recently developed by Mason et al. (2010). The child grid run was conducted after the parent grid integration (off-line); the parent grid conveyed initial and boundaries conditions to the child grid, but no information was passed back from the child to the parent grid (one-way). The forcing fields were analogous to the ones in the parent run except for using daily-varied data instead of monthly. The nested run was performed from April 1 to May 31, 2005. A set of 75,398 Lagrangian particles were uniformly deployed in the child grid in the surface layer on April 26 and their trajectories tracked for one month (the top layer in this case had variable depth due to the realistic bottom topography, but always less than 1 m and 0.2 m on average).

2.3 Results

2.3.1 The idealized set-up

The circulation in the idealized experiment is mainly horizontal and is characterized by a series of wind-induced coherent vortices embedded in the background turbulent field. Figure 2.2 shows a snapshot of vertical relative vorticity ζ scaled by planetary vorticity (i.e., by the Coriolis parameter f) in the surface and tenth layers, where particles are released, 60 days after their deployment. Relative vorticity, defined as $\zeta = \partial v / \partial x - \partial u / \partial y$, measures the local rotation rate in the horizontal plane. Positive values correspond to anticlockwise motion (cyclonic) and negative to clockwise (anticyclonic). The flow field has a pronounced dominance of long-lived anticyclonic vortices. At the surface,

submesoscale vorticity filaments are also visible around the eddies, while they are absent at depth. The asymmetry between anticyclonic and cyclonic vortices results from the straining field exerted by vortex Rossby waves (VRWs, Montgomery and Kallenbach, 1997), which induces a greater weakening of cyclones whenever the eddies have size comparable to the Rossby deformation radius, as in our simulation (Montgomery and Kallenbach, 1997; McWilliams et al., 2003; Graves et al., 2006). The average horizontal diameter of mature vortices is about 20 km, the average eddy turnover time is 3.2 days, and the Lagrangian time scale, i.e. a measure of the persistence of the fluid motion or the time required for a water parcel to be displaced from one location to another by the eddy field, is of 2 days at the surface and 3 days around 106 m, in agreement with oceanographic observations in regions with an energetic mesoscale (Lumpkin et al., 2002). In the vertical, the modeled eddies have a bowl-shaped vorticity signature extending to over 100 m and reduced intensity. The ratio ζ/f provides an estimate of the local Rossby number. In the vortex cores, the absolute value of ζ is about 1.5 times larger than f at the surface and only half the value of f at 106 m depth (Figure 2.2), implying that the surface motion within the eddies is strongly ageostrophic, while circulation at depth is closer to geostrophic balance also inside the vortices. In contrast to anticyclones, cyclonic vortices in this idealized run typically have a smaller radius, are confined to the mixed layer and are stretched out into filaments more rapidly.

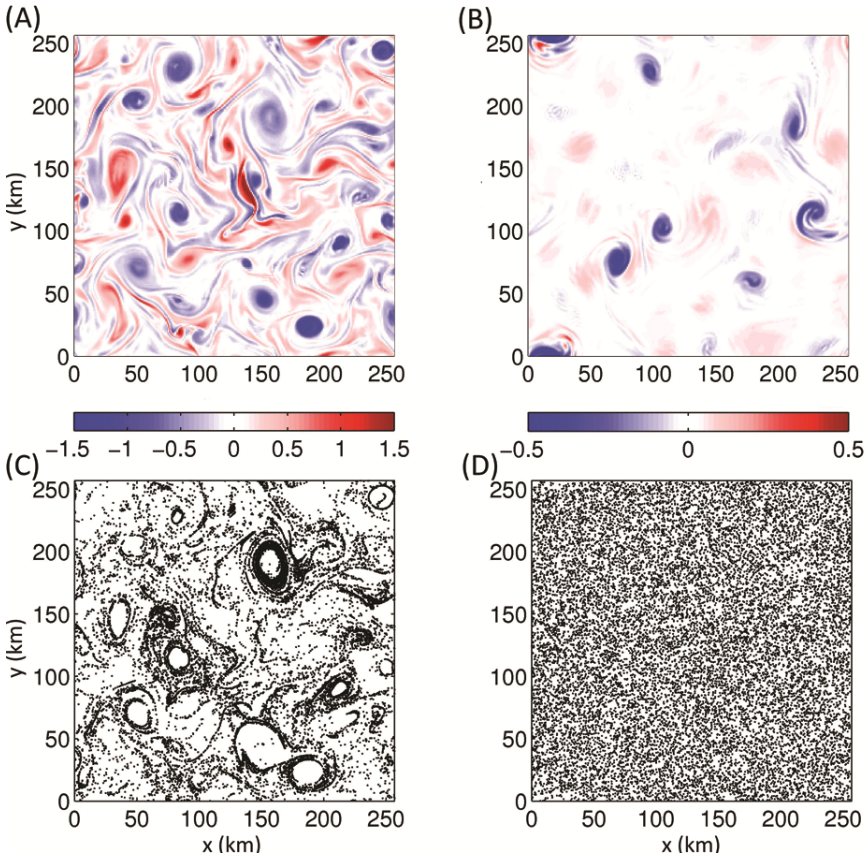

Figure 2.2: Relative vorticity scaled by the Coriolis parameter (ζ / f) at the surface (1 m, Panel A) and at 106 m (Panel B) in the idealized integration 60 days after particle deployment, and (Panel C and D) the corresponding particle distribution. Axes are in km.

To study the transport properties of this vortex-dominated flow, we deployed two sets of Lagrangian particles at different depths. The first set was released at about 1 m and represents a proxy of surface floating materials, whereas the second one released at 106 m, where the intensity of the vorticity field within the eddies is reduced to a third of the value at the surface. Each set contains 65,536 particles, initially sown uniformly over the entire domain. To highlight the role of vortices on particle distribution, we released a

second set of 32,761 particles homogeneously distributed inside one vortex, both at the surface and at depth. The edge of the vortex was defined as the closed contour line surrounding its core where the Okubo-Weiss parameter (*OW*) (Okubo, 1970; Weiss, 1991) is zero. *OW* measures the relative strength of local deformation and rotation. In 2-D and QG turbulence, this is defined as $OW = s^2 - \zeta^2$, where s measures the horizontal deformation due to stretching and shearing ($s^2 = (\partial u / \partial x - \partial v / \partial y)^2 + (\partial u / \partial y + \partial v / \partial x)^2$), and ζ is relative vorticity as mentioned above. In 3-D turbulence, as in our case, the horizontal components of the velocity tensors are at least one order of magnitude larger than the vertical component (10^{-4} vs. 10^{-5}), and the 2-D definition of *OW* still provides a clear horizontal separation between vortex-dominated and strain-dominated regions.

2.3.2 Mechanism of pattern formation

Figure 2.2 shows, in Panel C and D, the particle distributions after 60 days at the surface and deep levels. Tracers at the surface are no longer uniformly distributed but organized in *lines* and *rings*, with regions of very high and low concentrations, closely resembling the patterns seen in the satellite images of *Sargassum* (Figure 2.1). Particles aggregated and organized themselves soon after they were released (in less than two days). This behavior differs significantly from the one of Lagrangian tracers in 2-D or QG turbulence. Particles advected at depth, on the other hand, still maintain an almost uniform distribution, as in 2-D flows.

To understand the physical mechanism behind the different evolution of the particle trajectories, the velocity divergence/convergence field should be considered. For an incompressible fluid, the continuity equation ensures that

$$div(\mathbf{v}) = \frac{\partial u}{\partial x} + \frac{\partial v}{\partial y} + \frac{\partial w}{\partial z} = 0$$

where *u, v* and *w* are respectively the zonal, meridional and vertical component of the velocity **v** field. In 2-D or QG flows, the vertical velocity is null or constant, and the horizontal velocity divergence ($div_H = \partial u / \partial x + \partial v / \partial y$) is therefore zero. A tracer initially distributed uniformly will maintain its uniformity with time. In 3-D, on the other hand, the horizontal divergence/convergence field is determined by the vertical gradient of *w*. If such a gradient is small, i.e., in presence of vertical velocities that do not vary significantly with depth, then the particle behavior resembles the one of QG flows. This situation is recovered in our idealized simulations at any depth below 10 m from the surface, and follows from the ocean being a rapidly rotating, stably stratified flow. However, close to the surface, the velocity gradient is large. Vertical velocities are close to zero at the surface, while they are high immediately below the surface due to the presence of Ekman pumping, wind-driven vortices, submesoscale fronts, and vorticity filaments. Koszalka et al. (2009) introduced a diagnostic equation for *w* based on the horizontal flow divergence and analyzed all contributions. Using such formulation, it is possible to identify the terms contributing to the vertical velocity at and below the ocean surface. At the surface, the only term which is non-zero is the free-surface ($w = d\eta / dt$; here η is free surface). Immediately below the ageostrophic term

$$(-\int_z^\eta \alpha_1 \left[\frac{\partial \zeta_1}{\partial t} + u\frac{\partial \zeta_1}{\partial x} + v\frac{\partial \zeta_1}{\partial y} + w\frac{\partial \zeta_1}{\partial z} \right] dz - \int_z^\eta \alpha_2 \left[\frac{\partial \zeta_2}{\partial t} + u\frac{\partial \zeta_2}{\partial x} + v\frac{\partial \zeta_2}{\partial y} + w\frac{\partial \zeta_2}{\partial z} \right] dz \text{ , where}$$

$\zeta_1 = \partial v / \partial x$, $\zeta_2 = -\partial u / \partial y$, $\alpha_1 = (f + \zeta_1)^{-1}$, $\alpha_2 = (f + \zeta_2)^{-1}$), stretching

($-\int_z^\eta \alpha_1 [\chi_2 \zeta_1] dz - \int_z^\eta \alpha_2 [\chi_1 \zeta_2] dz$, where $\chi_1 = \partial u / \partial x$, $\chi_2 = \partial v / \partial y$) and tilting ($-\int_z^\eta \alpha_1 \left[\frac{\partial w}{\partial x} \frac{\partial v}{\partial z} \right] dz + \int_z^\eta \alpha_2 \left[\frac{\partial w}{\partial y} \frac{\partial u}{\partial z} \right] dz$) dominate the vertical velocity field and all display their maxima values, creating a very strong gradient.

Figure 2.3 shows the particle distribution overlying the local horizontal velocity divergence/convergence field at the surface with magnification of vortex *V*, whereas Figure 2.5 focuses on the tracers at 106 m. The horizontal velocity divergence/convergence balances the vertical velocity gradient and quantifies the rate of local fluid particle dispersion/accumulation; if negative, it represents convergence, while positive value indicates divergence. At the surface, most particles aggregate where convergence occurs (blue regions), while the divergence zones (in red) are left with a smaller number of tracers or almost vacant. Areas of strong divergence/convergence are found in and around the most intense vortices and submesoscale fronts, but do not correlate directly with the vorticity field. The divergence field, likewise *w* (Koszalka et al., 2009), is very complex, and results from the interplay of advection, stretching, and instantaneous vertical velocity changes. At the surface, the horizontal convergence field is so strong that surface particles show aggregation patterns about a day after deployment and tend to form circular rings at the vortices peripheries. The aggregation time scale at the surface is therefore shorter that the mean Lagrangian time scale (2 days) at which particles are advected by the eddy field. As a result, more particles are found in the blue regions at all times (Figure 2.4). Differences in the distributions shown in Figure 2.4 are related to the intrinsic variability of the eddy field given that eddies and vorticity filaments are continuously formed and destroyed in the idealized run in a chaotic manner.

During the 60 days during which the Lagrangian tracers are advected around, the total area occupied by eddies and strong filaments varies between 11% and 15.5%, and it is 12.5% on average. At 106 m, the intensity of the convergence/divergence field is reduced to ¼ or less of the surface values (the absolute value of the horizontal convergence averaged over the whole domain is five to six times smaller at 106 m than at the surface at all times), and the time required for aggregation is longer that the Lagrangian time scale (Figure 2.5). The horizontal convergence field at depth is therefore insufficient to drive particle aggregation. At depth, on the other hand, the horizontal velocities inside the eddies are much stronger than those in the background. As a result, for a few days after the release the particles trapped in the eddy cores can be identified by their twisting, faster motion (Figure 2.5). This may cause the (wrong) impression of particle aggregation for time scales shorter than the advective time of the background flow. As shown in Figure 2.6, particles are equally distributed in (weakly) positive and negative convergence regions at all times.

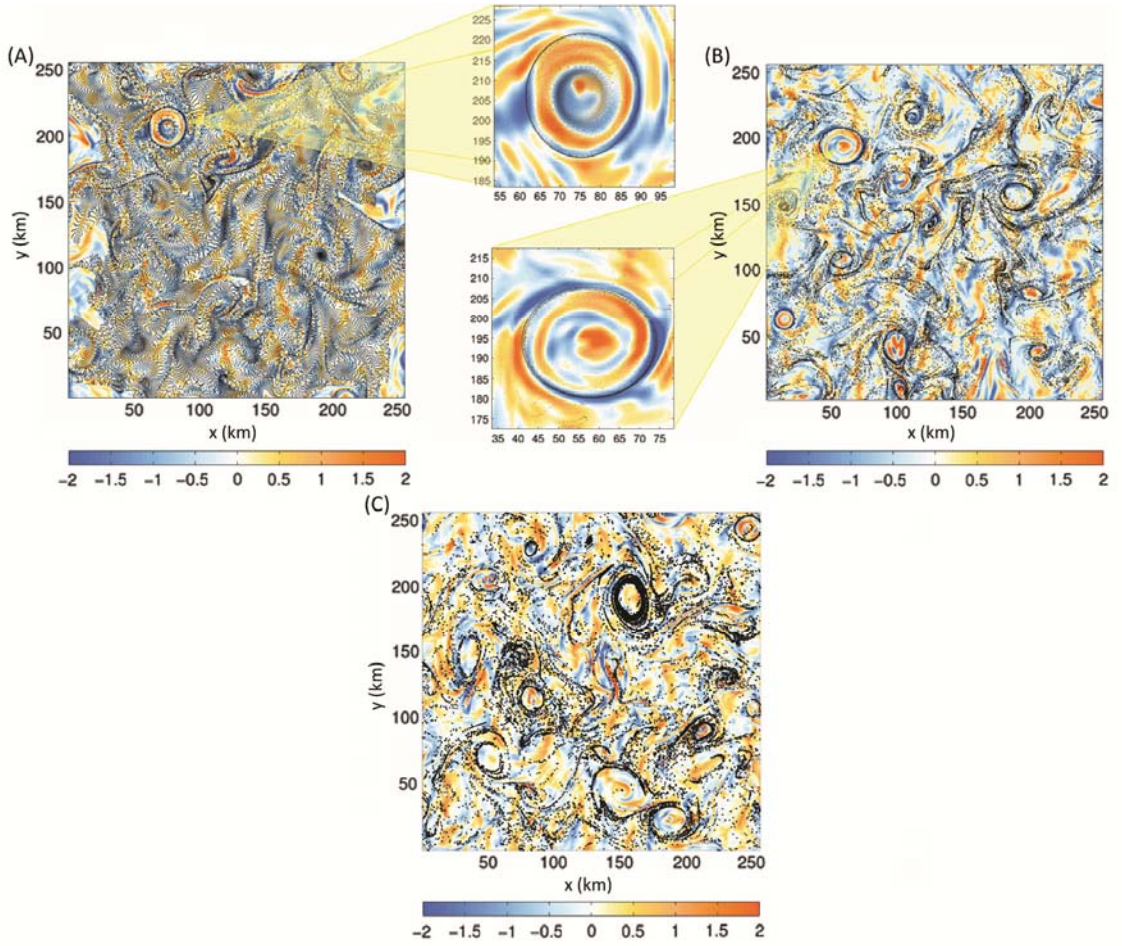

Figure 2.3: Distribution of Lagrangian particles deployed at 1 m depth after two days (Panel A), after two weeks (Panel B) and after 60 days (Panel C), with zooms on distributions of particles deployed inside one vortex overlying the horizontal divergence field (in color). The vortex is destroyed during a merging event after 40 days. Units of divergence field are $10^{-5}s^{-1}$.

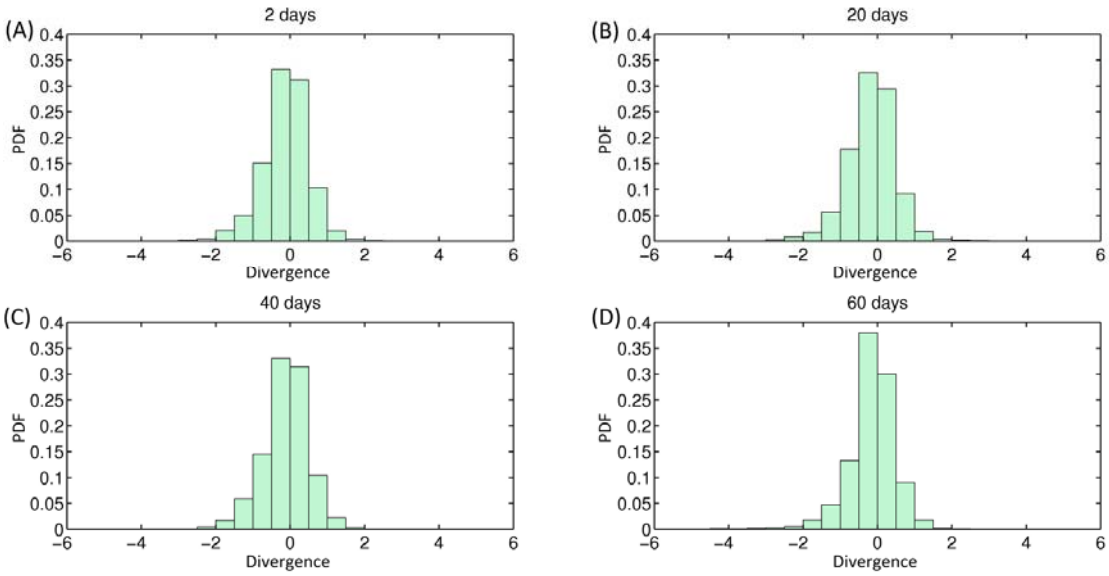

Figure 2.4: Probability of surface particles of falling into areas with different divergence values (aka PDF) at different time during the integration. The x-axis is divergence. (Unit: $10^{-5}s^{-1}$).

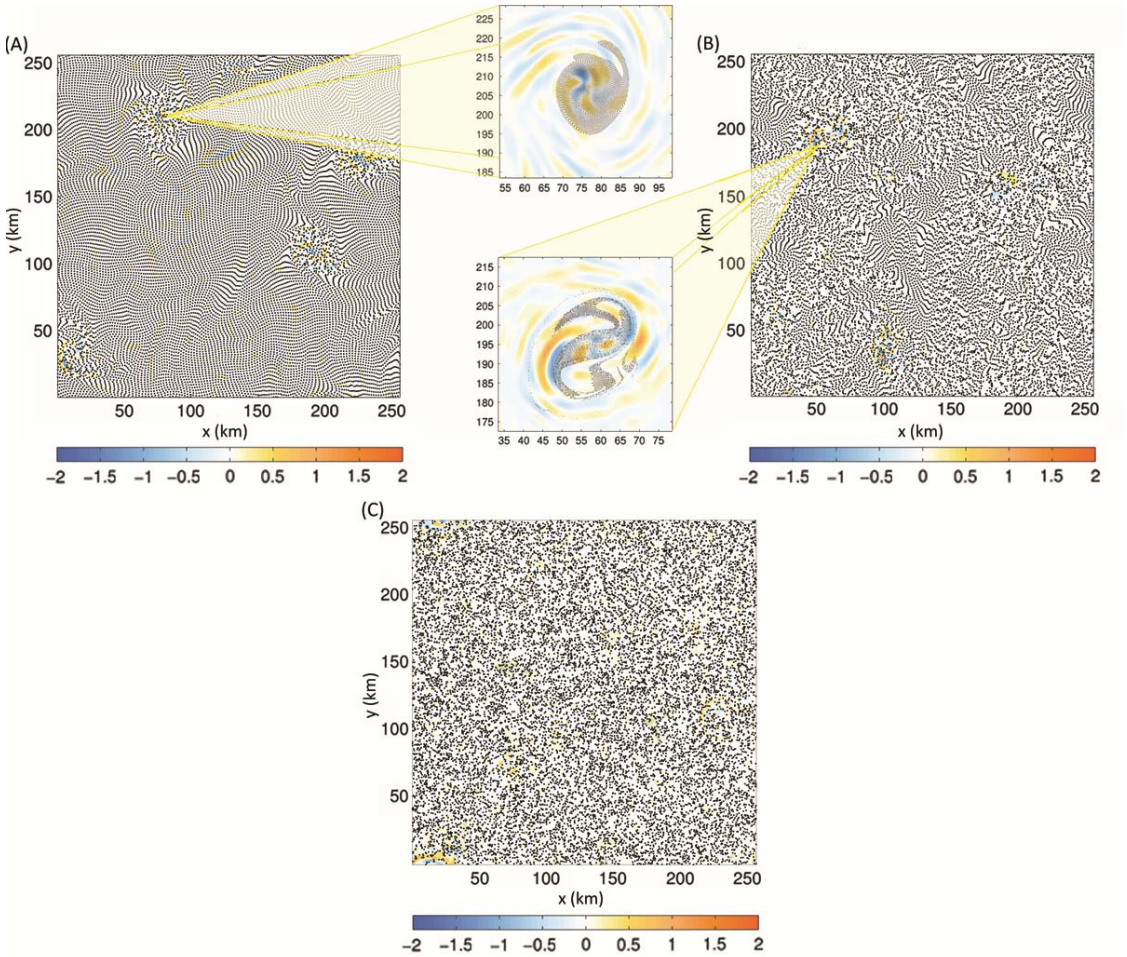

Figure 2.5: Same as in Figure 2.3 but for particles and divergence field at 106 m depth. The divergence field is plotted using the same color scale in Figure 2.3.

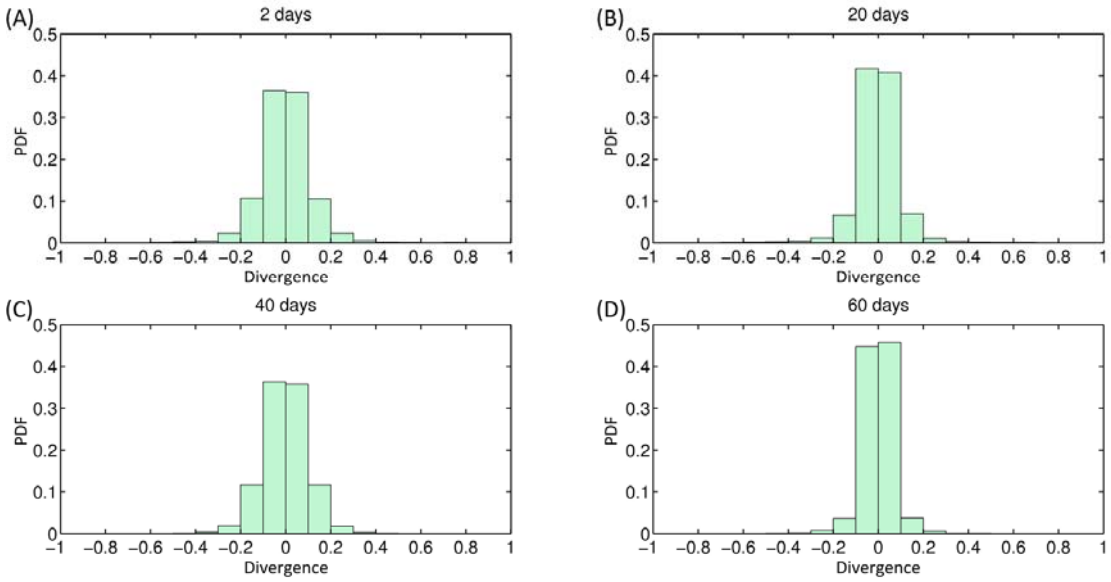

Figure 2.6: Same as in Figure 2.4 but for particles at 106 m depth.

2.3.3 Particle distribution at the ocean surface in the Gulf of Mexico

The idealized integration provides a theoretical framework to investigate particle distributions in a wind-driven, eddy-dominated ocean. It suggests that at the surface floating tracers aggregate following the horizontal divergence field, which is unusually strong due to the large gradients in the vertical velocity field in correspondence to submesoscale ageostrophic processes in vortices, vorticity filaments, and submesoscale fronts.

Figure 2.7 shows a snapshot of the surface relative vorticity field in the western Gulf of Mexico (scaled by Coriolis parameter *f*, counterpart of Figure 2.2) on May 1, 2005 in

the nested area where the horizontal resolution is 1 km. We are not performing any data assimilation and the physical processes responsible for eddy formation and propagation in the Gulf are to a large extent chaotic, so a direct comparison between data and modeled mesoscale features is not possible. Nonetheless, the run reproduces extremely well the sea surface height variance observed in satellite data and vorticity values are realistic. The vorticity field displays more complicated but overall slightly weaker patterns than in the idealized integration. We have chosen May 1, 2005 because of the many eddies of different sizes as well as numerous filaments and submesoscale fronts that can be identified in the vorticity map. Four areas with pronounced mesoscale/submesoscale features are labeled with *A*, *B*, *C* and *D* and they represent all the different patterns that can be found in the chosen domain. The three largest eddies seen in our domain (*B*, *C* and *D*) are originated from the Loop Current that enters the Gulf of Mexico between Cuba and the Yucatán peninsula, loops west and south and then exits through the Florida Straits. Its instability generates eddies at irregular intervals of 9-14 months that have typical diameters of 150-300 km and extends up to 1000 m in depth (Vukovich, 1995; Sturges and Kenyon, 2008). Newly formed eddies move westwards with a speed of about 2-5 km/day and can exist for months to years until they decay through the interaction with the continental shelf (Elliott, 1982; Vukovich and Crissman, 1986). When the Loop Eddies reach the Mexican continental shelf, they generally break up into smaller eddies generating dipole or, more rarely, tripole structures. Numerous small coherent vortices, generated independently of the Loop Current, are also resolved in our nested experiment. Their formation is by baroclinic instability associated with lateral boundary friction and bottom topography (e.g., the train of eddies along the

continental shelf on the west of the domain), or by baroclinic instability of the density fronts surrounding the Loop Eddies (e.g., region *A* in Figure 2.7). The intensity of both the vorticity and horizontal divergence/convergence fields varies within the different dynamical structures. The two regions with highest values are found in correspondence of *A* and *B*. *A* includes submesoscale eddies and filaments, whereas *B* is an anticyclonic eddy with diameter of approximately 200 km. The remaining two Loop Eddies (*C* and *D*) show a more homogeneous structure at their interior and lower intensity in the divergence/convergence field.

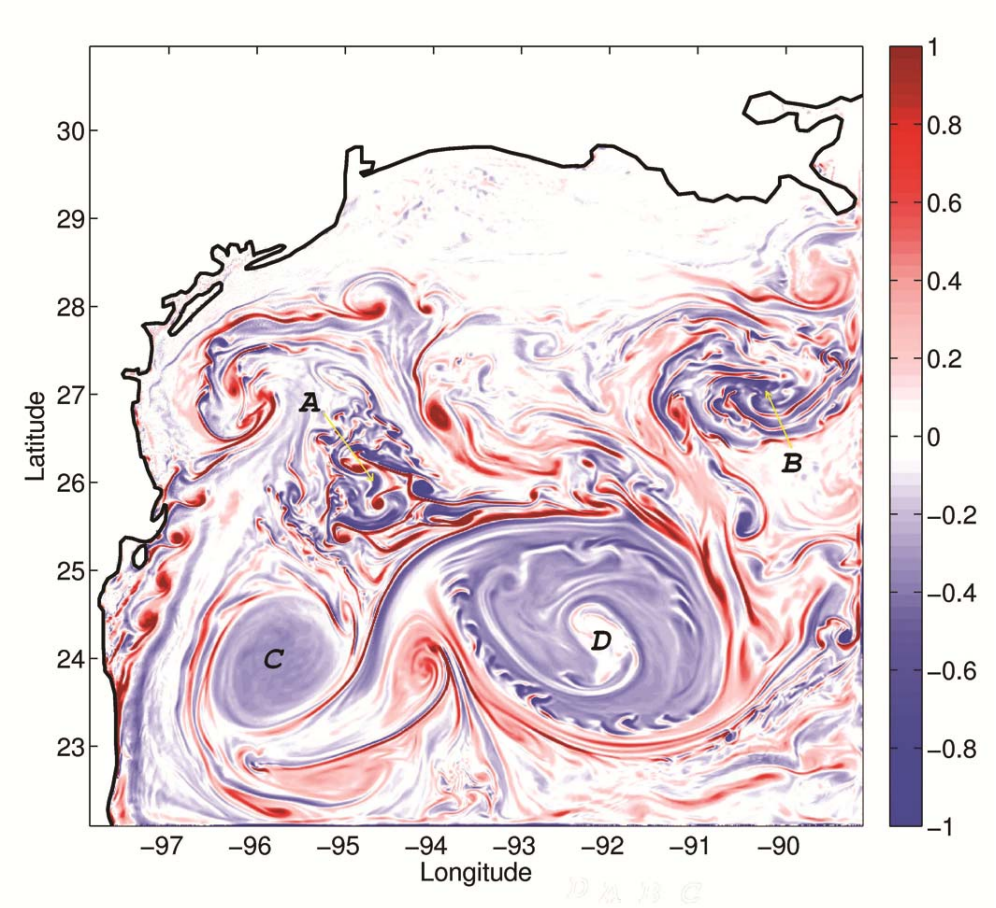

Figure 2.7: A snapshot of surface relative vorticity scaled by the Coriolis parameter (ζ/f) in the western Gulf of Mexico in May. The four regions described in the text are marked *A* to *D*.

To investigate the transport properties of this flow field, we deployed a set of 75,398 passive Lagrangian particles in the surface model layer over the whole domain on April 26, 2005. The tracers are initially distributed homogeneously. The distance between two neighboring particles is 30 km. Figure 2.8 displays the particle distribution five days after deployment superimposed to the convergence field. As in the idealized case, particles

rapidly aggregate to form patterns resembling curls and lines. Curls are particularly evident in regions *A* and *B* and are associated with comparatively strong vorticity and convergence/divergence fields. This kind of pattern is also captured by the satellite image shown in Panel B of Figure 2.1. Particle aggregation along lines mostly occurs in the enhanced submesoscale frontal regions, as for example on the edge of the weak eddies *C* and *D*. Those lines may extend to several hundred kilometers. Panel A in Figure 2.1 shows a satellite image of analogous 'lines' formed by *Sargassum* in the same year of our simulation. Snapshots of regions *A* and *B* confirms that most of the particles concentrate in the convergence zones (blue shading) forming the characteristic patterns due to the strong vertical velocity gradient of the flow at the ocean surface (Figure 2.9).

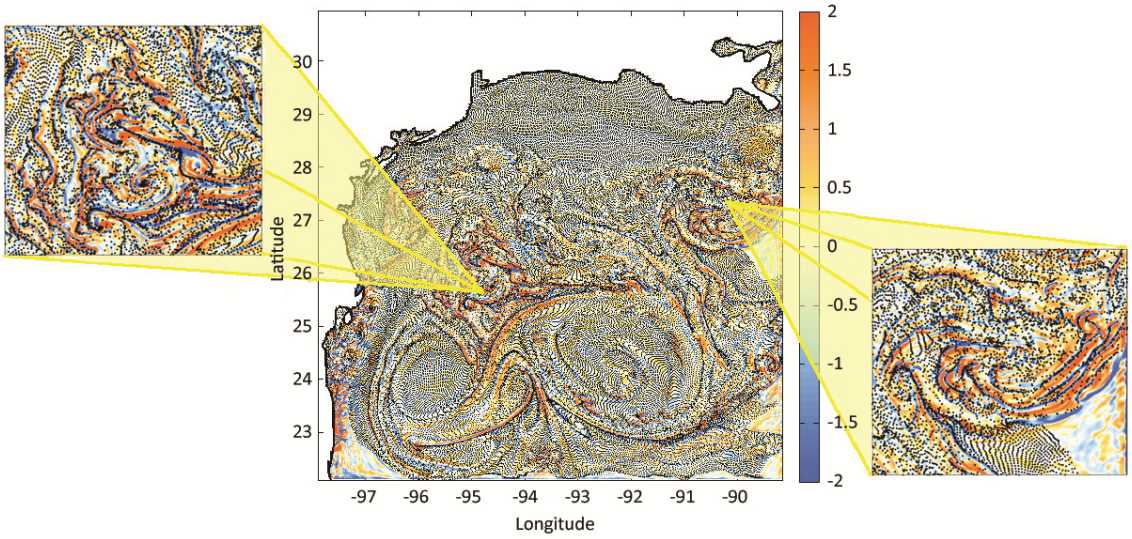

Figure 2.8: Distribution of surface Lagrangian particles overlying the horizontal divergence field (in color, Unit: $10^{-5}s^{-1}$) in the western Gulf of Mexico on May 1, 2005, with zooms on Region *A* and *B*.

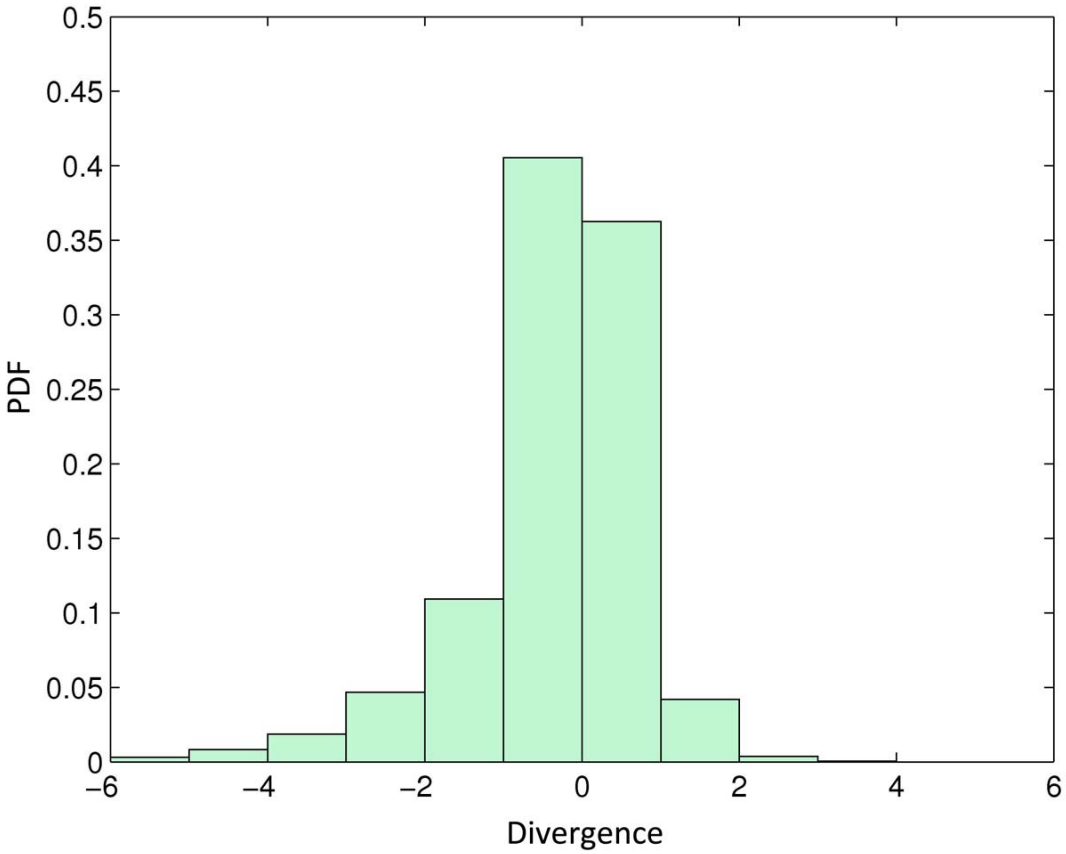

Figure 2.9: Probability of surface particles of falling into areas with different divergence values in the western Gulf of Mexico on May 1, 2005. The x-axis is divergence. (Unit: $10^{-5}s^{-1}$).

At 100 m depth, the vorticity field is highly correlated with the surface one, as expected based on the vertical extension of the Loop Eddies (Figure 2.10). Submesoscale vorticity patterns are also recognizable. However, the intensity of the vorticity scaled by the Coriolis parameter is comparable to the idealized simulation and everywhere less than

unity, indicating that the dynamics is not dominated by ageostrophic processes, and the convergence field is too weak to generate any particle accumulation.

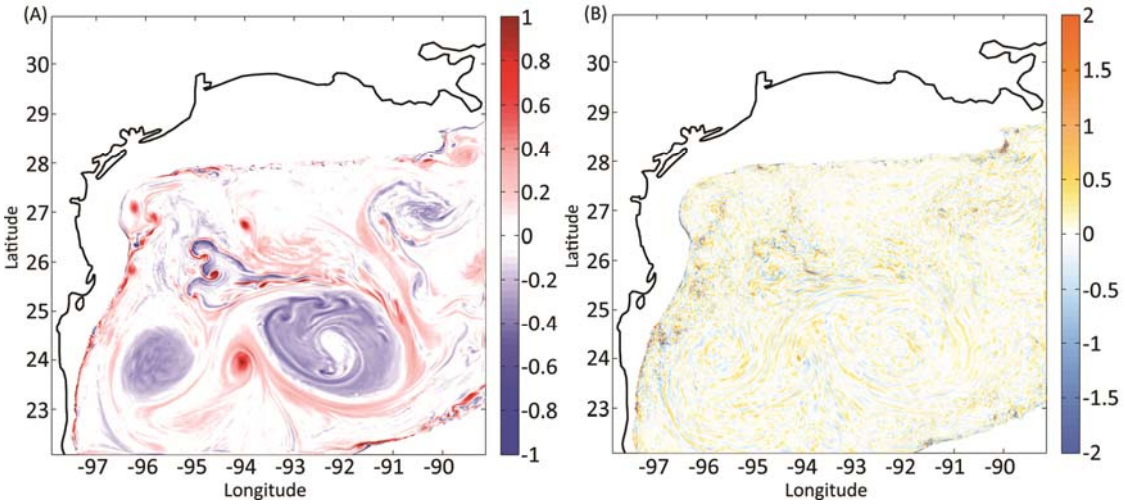

Figure 2.10: (A): Relative vorticity scaled by Coriolis parameter and (B): divergence field at 100 m depth in the Gulf of Mexico. (The unit for the divergence is 10^{-5} s^{-1}).

Whereas *Sargassum* blooms in the Gulf of Mexico are predominately observed in spring and early summer (March to July, Gower and King, 2008), the horizontal divergence/converge field contributes to pattern formation at the ocean surface all year around. In Figure 2.11, we present the outcome of a separate experiment run with the same set-up but 2 km horizontal resolution and over a domain covering the whole western Gulf of Mexico. 40,955 Lagrangian floats were deployed on January 27, 2004

and their trajectories were integrated for one month. A long-lived large Loop eddy, with a turnover time of about 7 days, dominates the mesoscale field in this simulation and displays a complex horizontal divergence field that causes the particles to aggregate along the convergence at its interior, again with patterns in agreement with the satellite observations.

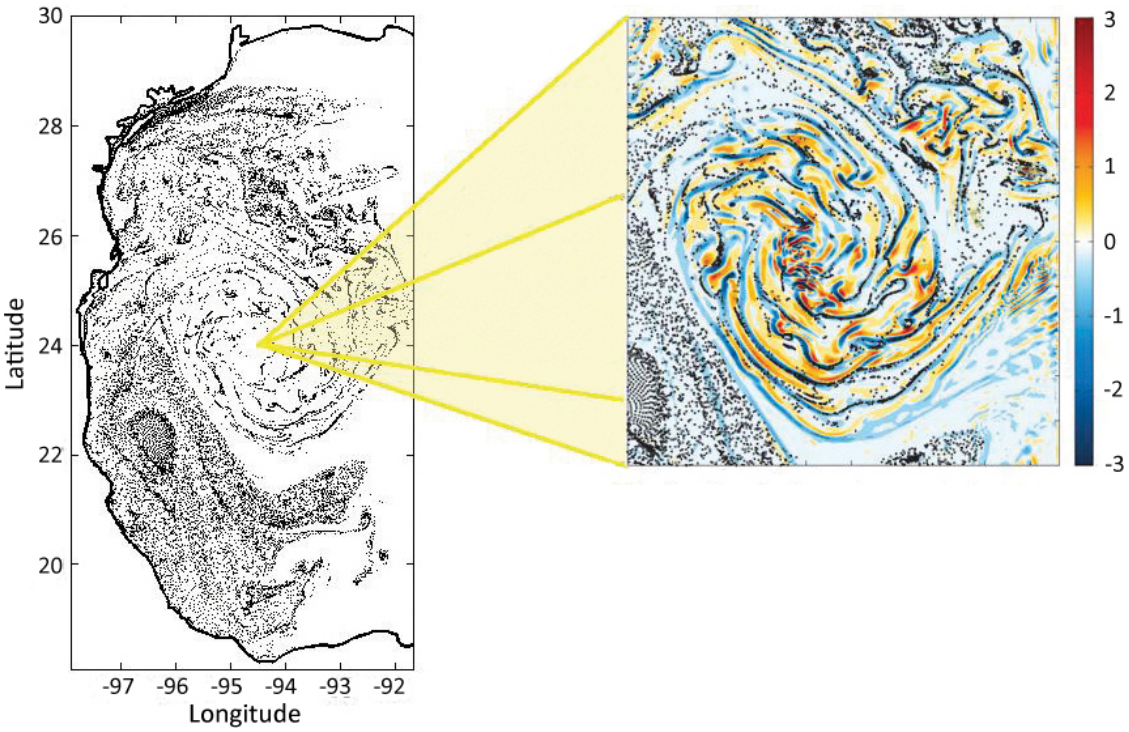

Figure 2.11: Distribution of surface Lagrangian particles in the western Gulf of Mexico on February 26, 2005, with a zoom over the large Loop Eddy overlying the horizontal divergence field (in color; Unit: $10^{-5}s^{-1}$). The horizontal resolution of this run is 2 km.

2.4 Conclusion and Discussion

In this chapter, we investigated how passive tracers are advected at the ocean surface using a regional ocean model run at high spatial resolution. Results have been qualitatively compared to satellite images capturing the *Sargassum* distribution at the ocean mesoscales. Both idealized and realistic model outputs strongly suggest that the highly heterogeneous patterns seen in *Sargassum* distribution at scales of kilometers are due to horizontal convergence/divergence patterns associated with submesoscale ageostrophic processes (McWilliams et al., 2009a, 2009b). The horizontal convergence field is particularly intense at the ocean surface to balance the strong vertical gradient of w, and it weakens rapidly below it. As a result, particle distributions at depth do not display any systematic heterogeneity. The stronger the surface horizontal convergence field is, the faster the particles aggregate. For weak convergence/divergence values, the time required to accumulate the particles is longer than the Lagrangian time scale, and particle distribution resemble those found in 2-D turbulence studies. According to our numerical simulations, patterns become recognizable when the model horizontal grid size is finer than 2 km and the temporal resolution of the momentum forcing is at least daily. Such a threshold may be model dependent as the parameterizations used for subgrid vertical and horizontal mixing may have a direct impact on the representation of the convergence/divergence field. The high horizontal resolution is required to properly resolve the structure of the submesoscale circulation. The wind field must contain energy at the inertial frequency (or higher) to excite quasi- and near-inertial motions in the vertical velocity, and therefore high values of w below the surface (Cardona and Bracco, 2011).

The Lagrangian tracers adopted in this work are neutrally buoyant and infinitesimally small. *Sargassum*, however, is slightly buoyant, has a finite size and will eventually sink due to epiphytic ballasting and buildup of vegetative (non-buoyant) growth. Particles with buoyancy that differs from the surrounding fluid and with finite size are subject to a complex suite of forces (see Maxey and Riley, 1983 for the full equation describing their motion) and their behavior may differ dramatically from the one of neutral tracers. If the particle size is less than the mean free path in the ambient fluid, the two dominant forces influencing the particle motion are the Stokes' drag (i.e., the friction that the fluid exerts on a particle moving with a velocity that is different from the fluid one), and the force that the fluid would exert on a fluid particle placed at the particle position, weighted by the relative inertia (i.e., the ratio of the fluid density to the density of the individual particle) (Crisanti et al., 1992; Tanga and Provenzale, 1994; Bracco et al., 1999). To verify that our conclusions are relevant to *Sargassum*, we modified the tracer equation in ROMS to include the two forces above following Tanga and Provenzale (1994) and we considered small spherical particles up to 10% lighter than the surrounding fluid. The resulting equation is a 2^{nd} order ordinary differential equations and its numerical convergence is achieved only with a very small time-step whenever in presence of an energetic advective field. Since the computational time required to advect buoyant tracers is at least one order of magnitude greater than the time required to advect neutral particles, we tested the robustness of our results only in the idealized configuration. We did not find any significant difference when comparing the patterns of neutral versus slightly buoyant tracers, and we verified that the forces acting on the particles do not contribute to the pattern formation.

As proxy for Lagrangian particles, *Sargassum* provides a readily visible buoyant tracer for the aggregation process. By extension, any particle-like organism at the ocean surface would be concentrated by this mechanism as well. This would include fish eggs, larval forms, surface-dwelling zooplankton such as pontellid copepods, siphonophores such as *Physalia* and *Vellela*, floating anthropogenic debris, and various components of the sea surface microlayer. Whereas our model does not incorporate growth, grazing or migration into/out of this region, and only describes the behavior of a collection of small individuals – large *Sargassum* patches probably act as a unit, it provides a first-order, easily testable mechanism for focusing biological interactions. Large-scale patterns seen in *Trichodesmium* blooms also exhibit aggregation along curls and lines similar to those seen in the model (Subramaniam et al., 2002; Sarangi et al., 2004). For positively buoyant particles, this organization scales of tens of kilometers and persistent from weeks to months – depending on the eddy lifetime – would be superimposed on top of Langmuir cell concentration at scales of tens of meters.

Our findings imply that at the ocean surface the strong horizontal divergence and convergence zones generated by ageostrophic processes at scales between hundreds of meters and a few kilometers are responsible for the creation of 'lines' where the floating material accumulates. The resulting patterns are similar to the distribution of *Sargassum* seen in satellite images and such organization is likely common in many surface dwelling organisms (neuston). Patches as described in this work will quickly form even in the event of uniform upward supply of the surface layer and then persist for a considerable time.

CHAPTER 3

SUBMESOSCALE IMPACTS ON HORIZONTAL AND VERTICAL TRANSPORT

Published as:

Zhong, Y. and A. Bracco. Submesoscale impacts on horizontal and vertical transport in the Gulf of Mexico. *J. Geophys. Res.*, 118: 1-18, 2013

Abstract

Impacts of submesoscale processes on transport are investigated numerically in an energetic mesoscale flow with an ocean model run at two horizontal resolutions, 1 km and 5 km. The focus is the northwestern Gulf of Mexico, where the Loop Current eddies are surrounded by smaller vortices. By increasing the horizontal resolution, the number and strength of submesoscale eddies and vorticity filaments within the mixed layer increase dramatically, and with them the vertical velocities. Inside the coherent eddies and at their peripheries increased vertical velocities for increasing resolution are associated with near inertial motions and they are not limited to the mixed layer, but are found at all depths. Horizontal velocities, on the contrary, are similar.

Lagrangian isobaric tracers are deployed close to the surface and at 100 m, and three dimensional, neutrally buoyant particles are released close to the surface, at the base of

the mixed layer and at 100 m. The modeled horizontal dispersion curves for each deployment depth are independent of the kind of particles and of horizontal resolution. Close to the ocean surface, however, convergence zones, generated by submesoscale ageostrophic motions and resolved at 1 km resolution, influence the details of the tracer distributions.

Vertical dispersion increases several fold for increasing resolution at all depths explored, with the largest differences found close to the surface. Therefore, submesoscales processes play a fundamental role in driving vertical transport in eddy dominated flows, both within and below the mixed layer, for times comparable to the Eulerian time scale.

3.1 Introduction

Ocean transport is an essential process occurring at all scales. In previous studies, a large body of work has focused on meso- and large scale transport. Submesoscale processes, due to their ephemeral nature, are difficult to sample accurately in field studies (D'Asaro et al., 2011; Li et al., 2012). However, theoretical and numerical works have showed the pervasive presence of submesoscale features at the ocean surface (Mahadevan and Tandon, 2006; Capet et al., 2008a; b; c; Thomas et al., 2008; Gildor et al., 2009; Klein and Lapeyre, 2009; Zhong et al., 2012). These features are characterized by large Rossby numbers, and are associated with enhanced mixing and strong vertical velocities ($O(10^{-4})$ m/s). They provide a pathway for energy transfers from the atmosphere to the base of the mixed-layer (Fox-Kemper et al., 2008; Mahadevan et al., 2010) and possibly to greater depths (Capet et al., 2008c; Koszalka et al., 2009), for

enhanced air-sea fluxes, and for the advection of biological tracers (Lévy et al., 2012). Submesoscale phenomena appear to be key players in regions characterized by mesoscale features. For instance, submesoscale fronts often emerge alongside energetic boundary currents and strong density gradients (Mahadevan and Tandon, 2006; Capet et al., 2008b; Klein et al., 2008; D'Asaro et al., 2011). In model simulations, local areas of strongly ageostrophic motion have been found also within and around eddies (Koszalka et al., 2009; Koszalka et al., 2010; Zhong et al., 2012). However, the relationship between submesoscale and mesoscale motions and their temporal and spatial interplay have not been studied in detail, and little is known of the impact of motions at scales of the order of O(1) km in regions characterized by the presence of long-lived mesoscale eddies.

In this chapter, we focus on an area with elevated eddy activity but no permanent frontal systems, the northwestern Gulf of Mexico. Our objective is to investigate numerically how the inclusion of submesoscale processes impacts horizontal and vertical transport in the water column. We do so by analyzing the Eulerian properties of the flow and the absolute dispersion of neutrally buoyant Lagrangian particles in two integrations at different resolution. In the Gulf of Mexico, the ongoing experiment Grand Lagrangian Deployment (GLAD) under the CARTHE (Consortium for Advanced Research on Transport of Hydrocarbon in the Environment) project (http://www.carthe.org/glad) aims at evaluating horizontal transport and mixing at the submesoscales using a large number of drifters. It will therefore provide an observational counterpart to the analyses presented here. Direct measurements of vertical transport and mixing in the ocean, on the other hand, are virtually impossible with current instruments, and indirect estimates from microstructure techniques are few and localized (Toole et al., 1994; Polzin et al., 1997;

Ledwell et al., 2000). From a modeling standpoint, estimates of ocean vertical dispersion may depend greatly on the vertical mixing parameterization scheme used and approximations made. For example Smith and Ferrari (2009), using a quasigeostrophic model and following previous work by Klein et al. (1998), have shown that in a flow with a fixed stratification and without any parameterized vertical mixing, eddy stirring represents an avenue for compensated vertical temperature and salinity (T-S) gradients. Molemaker et al. (2010), on the other hand, with a primitive equation model have identified a colocation of T and S gradients and elevated mixing in submesoscale fronts, and an increase in the amplitude of such gradients with increasing model resolution.

Here we implement a primitive equation model to quantify vertical dispersion within and immediately below the mixed layer, which is of scientific interest for the parameterization of vertical diffusion in coarse resolution models, and also important for understanding the vertical exchange of biological tracers (Lévy et al., 2012).

3.2 Model and Configuration

The numerical model implemented is the Regional Ocean Modeling System (ROMS). ROMS is a 3-D, free-surface, hydrostatic, primitive-equation circulation model with a generalized vertical terrain-following coordinate (Shchepetkin and McWilliams, 2005). The model is initially configured over the whole Gulf of Mexico with horizontal resolution of 5 km and 30 vertical layers (LR for lower resolution). At least 9 of those layers, and on average 15, are concentrated in the first 150 m. The atmospheric forcing fields include six-hourly wind stresses from QSCAT/NCEP blended dataset (Chin et al., 1998; Milliff et al., 2004), and six-hourly net heat, fresh water and solar radiation fluxes

from NCEP/NCAR reanalysis (Kalnay et al., 1996). At the model boundaries, monthly-varying Simple Ocean Data Assimilation (SODA, Carton and Giese (2008)) reanalysis is used. To guarantee a statistically stationary initial state, the model is first spun up for ten years, using SODA as initial and boundary conditions, with NCEP/NCAR monthly varying forcings averaged over the 1948–2002 period. ROMS is then run as described above from 2002 to 2005. On January 1, 2005 we begin a one-way offline nesting integration on a 1 km × 1 km horizontal resolution grid (HR for high resolution) covering the north western side of the basin from 98°W to 89°W and 22°N to 31°N (see *Mason et al.*, 2010 for details on the nesting procedures). We focus the subsequent analysis in this area.

The dynamics on the western side of the Gulf are characterized by the presence of large anticyclones, so called Loop Current eddies or Rings, with diameter of 200–300 km on average, and a vertical extension up to 1000 m (Cooper et al., 1990; Forristall et al., 1992). The Rings detach from the Loop Current at irregular intervals of 9–14 months (Vukovich, 1995; Sturges and Kenyon, 2008), and their formation mechanism includes both a deterministic and a stochastic component. Overall, observed mean circulation and eddy kinetic energy levels in our parent grid are in good agreement with the observed ones (Zhong et al., 2012). The Rings detach from the Loop Current with a realistic frequency, but in most cases the timing does not coincide with observations, given that we are not performing any data assimilation. Newly shed Rings then move westwards, with a speed of 2–5 km/d, entering our domain of interest, and then often break up into smaller eddies. They may form dipoles or more rarely tripoles when interacting with the continental shelf, and their modeled life span is in good agreement with observations. A

number of smaller coherent vortices can be found along the Tamaulipas-Veracruz Shelf, close to the western boundary. For an extensive validation of both near surface and deep mesoscale circulation in a configuration similar to the one adopted here, the reader is referred to Cardona and Bracco (submitted to Deep Sea Research II, 2013). Modeled temperature and salinity profiles and modeled transport at the Yucatan Channel compare well with in-situ data. Salinity gradients at the base of the mixed layer and main thermocline are slightly underestimated by ROMS when compared to the World Ocean Atlas 2009 multi- year averages, but agree well with CTD (Conductivity, Temperature, and Depth) measurements collected during the Northeast Gulf of Mexico (NEGOM) program in 2000. The seasonal cycle and intensity of the surface geostrophic velocities, the interannual variability of the Loop Current and the Loop Current eddy shedding derived from altimeter measurements are also accurately represented.

The focus of this work is the transport, both horizontal and vertical, associated with the model representation of the eddies that populate the Gulf of Mexico within and below the mixed layer. To investigate the role of the submesoscales in the representation of such transport, we deploy over 100,000 passive, neutrally buoyant Lagrangian particles in both 1 km and 5 km simulations in an area of intense mesoscale activity, shown by the black rectangles in Figure 3.1, and we integrate their trajectories for 40 days, which is approximately the Eulerian time scale of the flow (Cardona and Bracco, submitted to Deep Sea Research II, 2013). The tracers are released close to the surface (5 m), at the base of the mixed layer (50 m, the mixed layer depth, defined by the maximum potential density gradient, is 54 m on average, and oscillates between 35 and 70 m during the time of the Lagrangian integration), and below the mixed layer (100 m), within the well

vertically resolved portion of the domain. Particles are homogeneously distributed within the box on a 1 km × 1 km grid. ROMS allows for integrating online neutrally buoyant Lagrangian trajectories, so that the temporal discretization errors associated to an offline deployment are avoided (Keating et al., 2011). The time evolution of each particle position is given as Equation 2.1. In that equation, the position vector can be three-dimensional (3-D), allowing the neutrally buoyant particles to move freely in the water column, or two-dimensional (2-D), limiting the particle motion on a horizontal plane. 2-D particles are confined to a fixed isobaric level and are representative of isobaric floats or drifters, commonly used in oceanic measurements. Due to our interest in vertical transport, we deployed 36,000 3-D particles at each of the depths indicated and at both resolutions; as comparative experiment we also released a set of 36,000 isobaric (2-D) particles close to the surface, at 5 m, and within the pycnocline layer, at 100 m in the two runs.

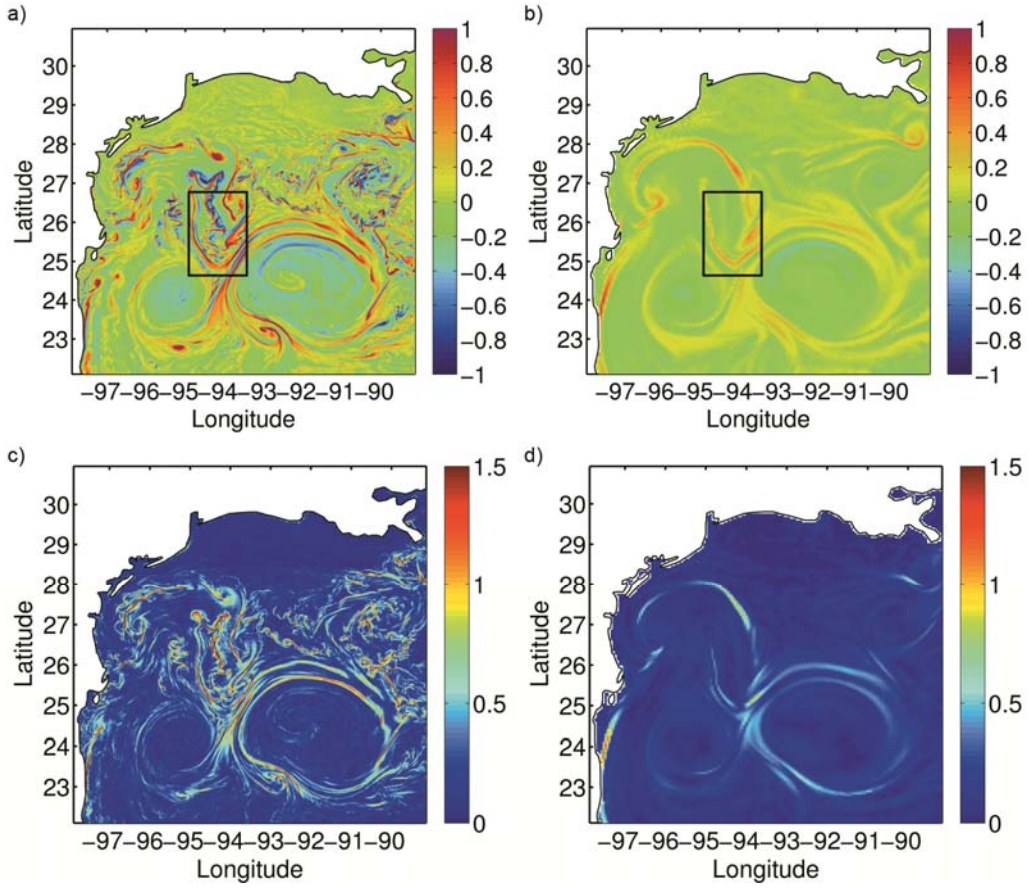

Figure 3.1: Snapshots of surface relative vorticity (top panels) and surface horizontal shear (bottom panels), scaled by the Coriolis parameter *f* on April 21, 2005. (a) and (c) 1 km nested run. (b) and (d) 5 km parent grid. The black boxes indicate where Lagrangian particles are deployed.

3.3 The Eulerian Flow

A comparison of the vorticity fields in the HR and LR integrations over the Gulf of Mexico shows similar mesoscale features (e.g. top panels in Figure 3.1 for a snapshot of

vorticity, ζ, normalized by the Coriolis parameter, f, to measure the local Rossby number, R_o, of the flow on April 21, 2005), with two large anticyclonic Loop Current eddies in the southern portion of the domain, and smaller mesoscale features to the north and east of the Rings. The evolution of the eddy kinetic energy (EKE) is also analogous (Figure 3.2).

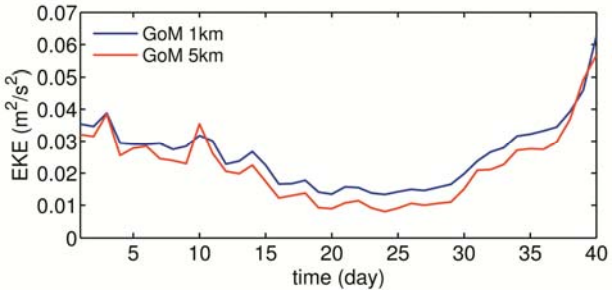

Figure 3.2: Time series of daily averaged eddy kinetic energy during the Lagrangian deployment period in the parent (red) and nested (blue) grids. The correlation coefficient between the two curves is cc = 0.98.

When comparing HR and LR vorticity fields, we find that the dynamics are dominated by eddies in both cases, while strong frontal structures, more commonly studied in the ocean submesoscales literature (Mahadevan and Tandon, 2006; Capet et al., 2008b; Klein et al., 2008; Thomas and Ferrari, 2008; D'Asaro et al., 2011), are absent. However, at 1 km resolution the flow at the submesoscale, as measured by the Rossby number, is more ageostrophic, and vorticity filaments easily undergo

submesoscale instabilities (Molemaker et al., 2005; Boccaletti et al., 2007; Thomas et al., 2008) with the generation of small coherent vortices, the often termed mixed layer eddies (Fox-Kemper et al., 2008), of radius varying between 3 and 20 km over most of the domain. The instability processes at play in the ocean when $R_o \sim$ O(1) are numerous, ranging from frontogenesis, easily identifiable by the large values of lateral strain rates, to ageostrophic baroclinic instability, and forced instabilities (by the atmospheric forcing, both momentum and heat fluxes). The ageostrophic baroclinic instability is often referred to as mixed-layer instability or ageostrophic anticyclonic instability, in relation to its balanced and unbalanced states, respectively, and the first one is responsible for the generation of the mixed layer eddies. A review of those processes is given in Thomas et al. (2008). In our realistic numerical set-up, their relative contributions vary in space and time continuously. The analysis of the local Rossby number of the flow and of its lateral strain rate (Figure 3.1c and 3.1d) reveals that spontaneous frontogenesis, found in regions where high R_o and high strain are co-located, is present between and immediately around the Loop Current eddies, as in the elongated filaments within the box where we deploy the Lagrangian tracers. In HR, those filaments are very thin, and they are characterized by O(1) Rossby number and high shear rate; in comparison, at 5 km resolution all structures appear smoother and less intense. Mixed layer eddies are more abundant in the western portion of the domain and to the north of the largest Ring, and they are absent in LR.

As already pointed out, the time evolution of the domain averaged EKE is common to the two resolutions, even if slightly larger in the 1 km case (Figure 3.2). The difference in energy content in the simulations is associated with the submesoscale flow resolved in

HR, but not in the LR integration. This is highlighted in the analysis of the horizontal kinetic energy spectra (Figure 3.3). In HR, the surface energy distribution follows a ~ k^{-2} regime at scales below 90 km, consistent with previous works at analogous resolution (Capet et al., 2008a,b; Klein et al., 2008) and observations (Ferrari and Rudnick, 2000; Le Traon et al., 2008). This power spectrum is indicative of local dynamics. In LR, the surface energy spectrum is steeper, and its slope is close to ~ k^{-3}, as expected for geostrophic turbulent flows (e.g. Bracco et al., 2004). In both runs, the spectral slopes increase slightly with depth, but remain flatter in HR than in LR.

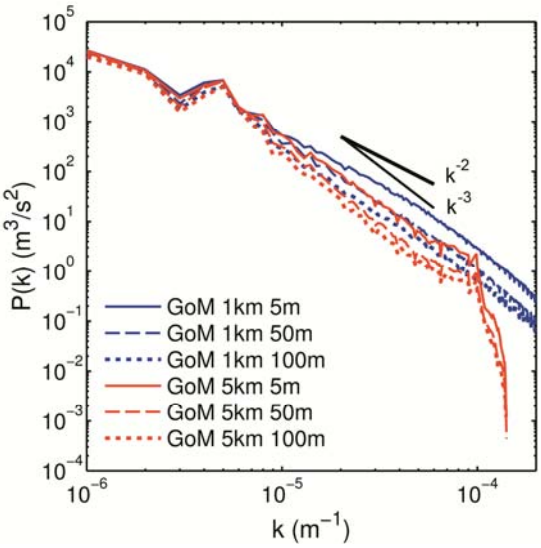

Figure 3.3: Azimuthally-integrated spatial power spectra of surface horizontal kinetic energy at the three deployment depths for the 1 km (in blue) and the 5 km (in red) resolution runs. (Unit: m^3/s^2).

The different slopes in the horizontal energy power spectra and slightly higher energy content in HR than in LR do not cause any detectable difference in the probability density functions (PDFs) of the horizontal velocities in the two integrations. We show, as example, the PDFs separately calculated for u and v at 50 m depth (Figure 3.4a). Almost identical distributions are found for the horizontal velocity components at any depth considered (5 m, 50 m, 100 m, 500 m, and 1000 m). While the shape is unaltered through the water column, the standard deviation decreases with depth (0.30 ± 0.01 m/s at the surface, 0.27 ± 0.01 m/s at 50 m, 0.25 ± 0.01 m/s at 100 m, 0.07 ± 0.01 m/s at 500m, and 0.04 ± 0.01 m/s at 1000m). The PDF of surface vorticity, on the other hand, displays a strong asymmetry with a long exponential tail for positive values at both resolutions, due to a predominance of cyclonic filaments (Figure 3.4b). The positive skewness increases with resolution (2.2 and 1.4 in HR and LR, respectively) due to the increase in strength of the filaments, and it is comparable to what found in previous modeling exercises (Capet et al., 2008a; Klein et al., 2008; Lévy et al., 2010). Note the difference in the tails also for negative vorticity, owing to the formation of strong anticyclonic filaments in HR in areas characterized by high shear away from the Loop Eddies (Figure 3.1c and 3.1d). At 100 m depth the shape of the vorticity PDF is similar to that of the surface, but the asymmetry is reduced at both resolutions (the skewness is 0.9 in HR and 0.6 in LR). The standard deviation is twice as large in HR as in LR at the surface, and 1.5 times larger in HR at 100 m.

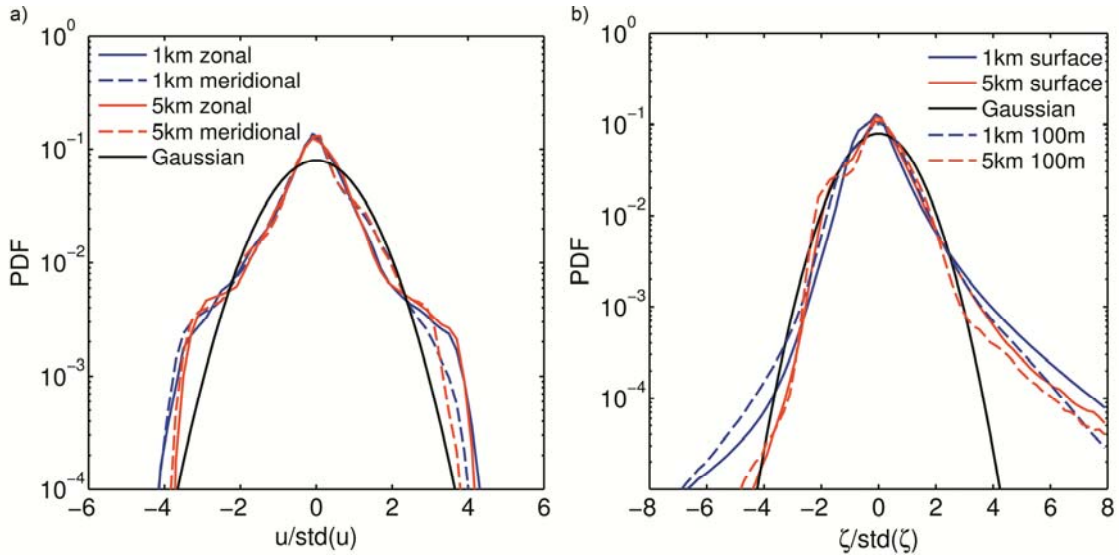

Figure 3.4: Panel (a): Probability density function (PDF) of Eulerian horizontal velocities at 50 m, normalized to have unit variance. Panel (b): PDF of relative vorticity at the surface and 100 m depth, normalized to have unit variance.

Moving onto the vertical circulation, the increased horizontal resolution in HR does not cause any relevant change in the representation of vertical stratification. Vertical profiles of temperature and salinity are analogous in the parent and nested runs. An example is provided in Figure 3.5a and 3.5b, where we plot the vertical sections of the modeled temperature field across 94.3°W averaged over two weeks (April 21 – May 4, 2005). Small differences are visible along the continental slope in correspondence to bathymetric features, given that HR is capable of better resolving the topographic roughness. Density spectra are analogous at all depths, and in the top 100 m of the water column follow a k^{-2} slope.

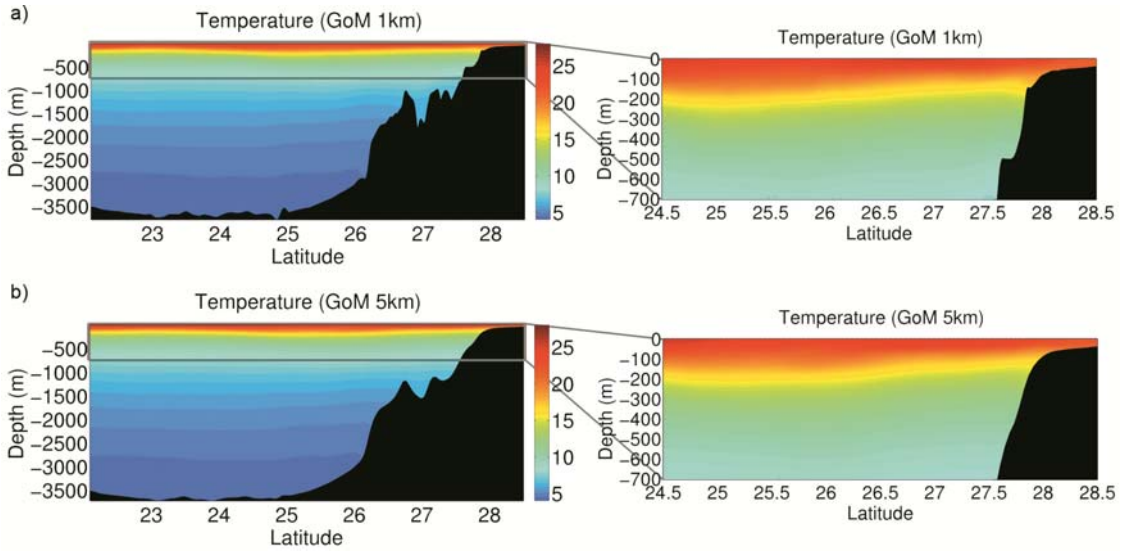

Figure 3.5: Transects of temperature along 94.3°W (where the Lagrangian particles are released) averaged over April 21–May 4, 2005, and zoom of the top 700 m of the water column. (a) 1 km and (b) 5 km resolution runs.

The vertical velocity fields, w, on the other hand, are very different in magnitude, despite the same vertical resolution. Differences between the two integrations are evident both in the instantaneous and in the time averaged w fields. Figure 3.6 and 3.7 show horizontal transects of w at 5 and 100 m in HR and LR, and compare instantaneous and 7-day (approximately six inertial periods) averaged fields. In the instantaneous fields (Panels a, b in both figures), values at least twice as large are found in the nested run compared to the parent simulation. This is true not only over the continental shelf, where inertial gravity waves generated over a better resolved topography could explain the higher values in the 1 km case, but also away from seamounts or canyons, in deep waters, far from the continental slope. Close to the surface, such increase is greater over regions

with modest topographic variations, but elevated submesoscale activity, at the edge of the Loop Current eddies and in correspondence with filamentary structures, is in agreement with previous findings. At 50 m and below (here we show 100 m), alternating regions of strong positive and negative vertical velocities are found in both the whole domain and particularly inside the Loop Current eddies, and are indicative of energetic near-inertial motions, as already shown by Koszalka et al. (2009) and later quantified by the frequency spectra in Figure 3.9b. Eddies are indeed capable of polarizing and transferring wind-forced near-inertial energy into the ocean interior (Kunze, 1985; Klein et al., 2004; Danioux et al., 2008, 2011). From a modeling prospective, such transfer is simulated only if the ocean model is forced with wind products containing energy at the frequencies to be excited (Klein et al., 2004; Cardona and Bracco, 2012) as in the present case (we use 6-hourly winds). Using Eq. 7 in Kunze (1985), it is immediate to see that the internal waveband broadens in regions of negative vorticity, and therefore inside the Loop Current eddies. It follows that in regions of negative vorticity near inertial waves have an intrinsic frequency lower than that of the surrounding ocean, and are unable to leave the vorticity trough (e.g. Shay et al., 2008). In regions of positive vorticity, on the other hand, the intrinsic frequency is higher than the effective Coriolis frequency, and the waves can freely propagate out. As a result, near inertial waves are usually trapped into anticyclones and expelled from cyclones, as confirmed numerically by Danioux et al. (2008). The background flow and/or the topography can further contribute to the intrinsic frequency and modify the behavior described above (Oey et al., 2008).

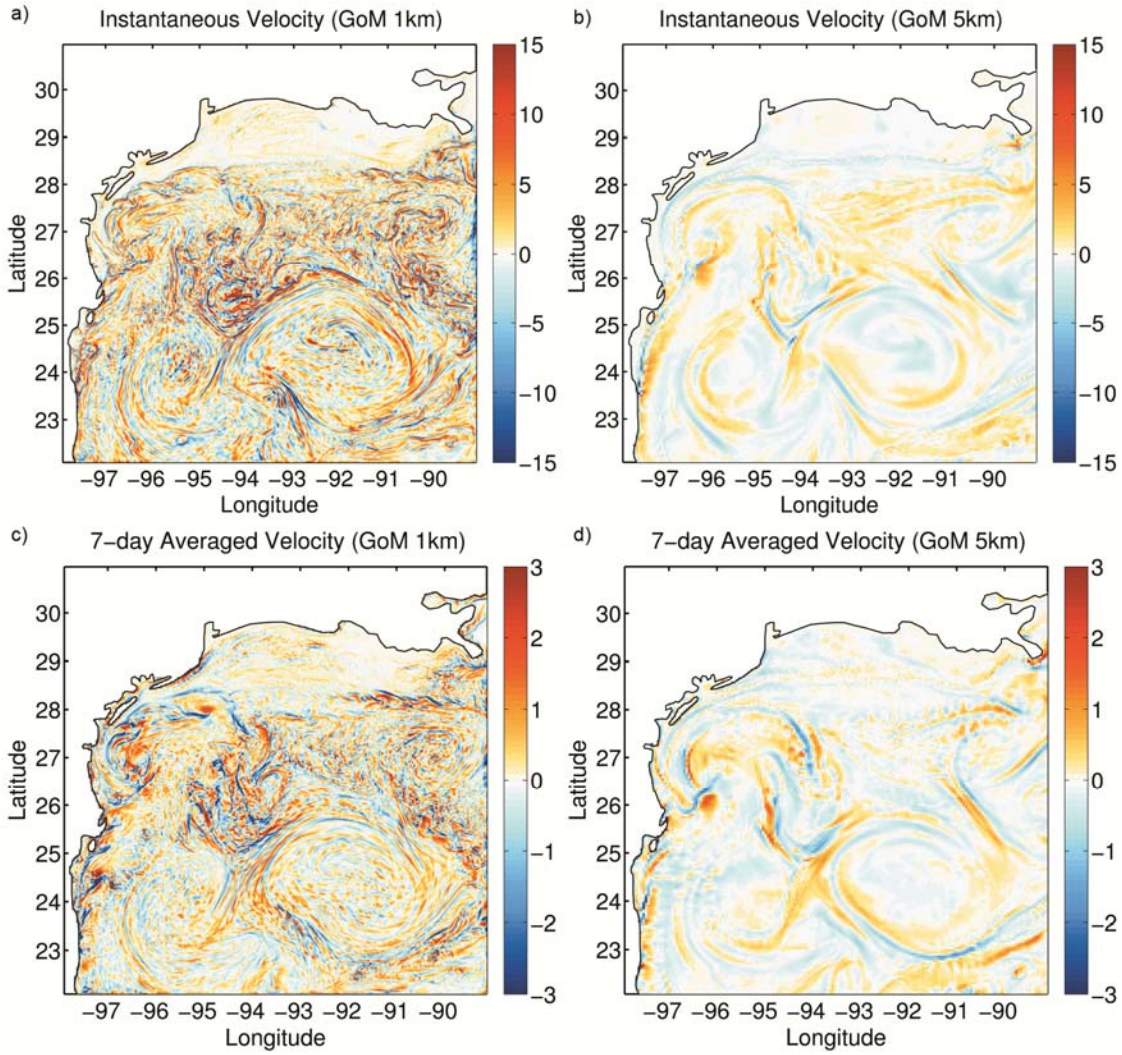

Figure 3.6: Instantaneous (a and b) and 7-day averaged (c and d) vertical velocity at 5 m depth. (a) and (c): 1 km resolution run; (b) and (d): 5 km resolution run. (Unit: m/day).

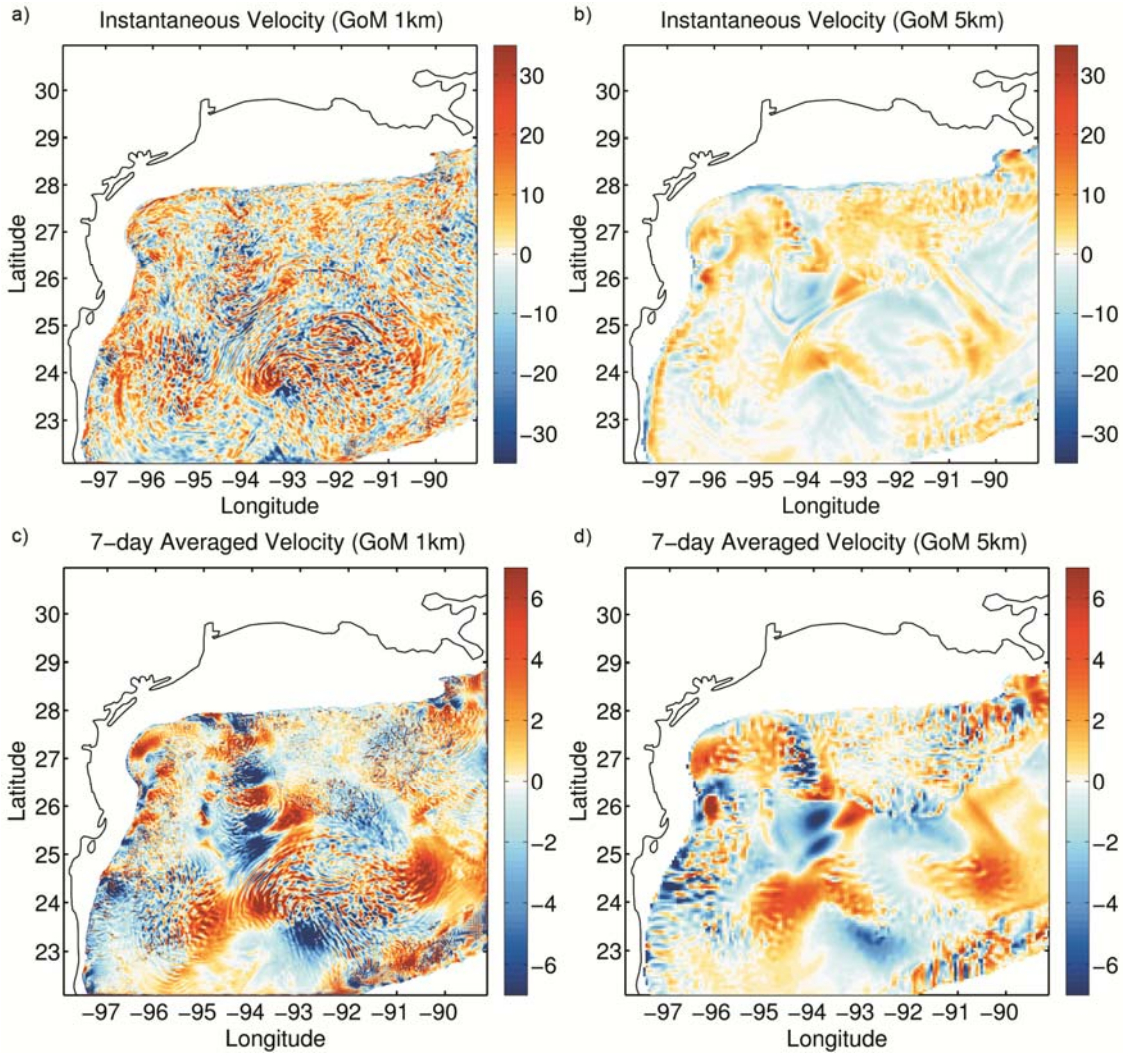

Figure 3.7: Same as in Figure 3.6 but for 100 m depth.

Whenever w is averaged over several inertial periods (Panels c, d in Figures 3.6 and 3.7), we notice a substantial increase in w amplitude and small scale complexity at higher resolution, but a good correspondence between mesoscale velocity patterns, especially at depth. Again, close to the surface the strongest velocities are found at the periphery of the

eddies and in regions where ageostrophic motions predominate. At 100 m most features found in HR can be seen also in LR, and major differences in patterns and intensity are seen inside the eddies.

The differences in instantaneous vertical velocities are mirrored in the horizontal density gradients (Figure 3.8), also more intense in HR than in LR, both at the surface and at depth, in agreement with previous works (Mahadevan, 2006; Nagai et al., 2006; Capet et al., 2008b), and in the spectra of the horizontal gradient of density for scales smaller than ~ 100 km, flatter in HR than in LR (the slopes are respectively close to k^{-1} and k^{-2}).

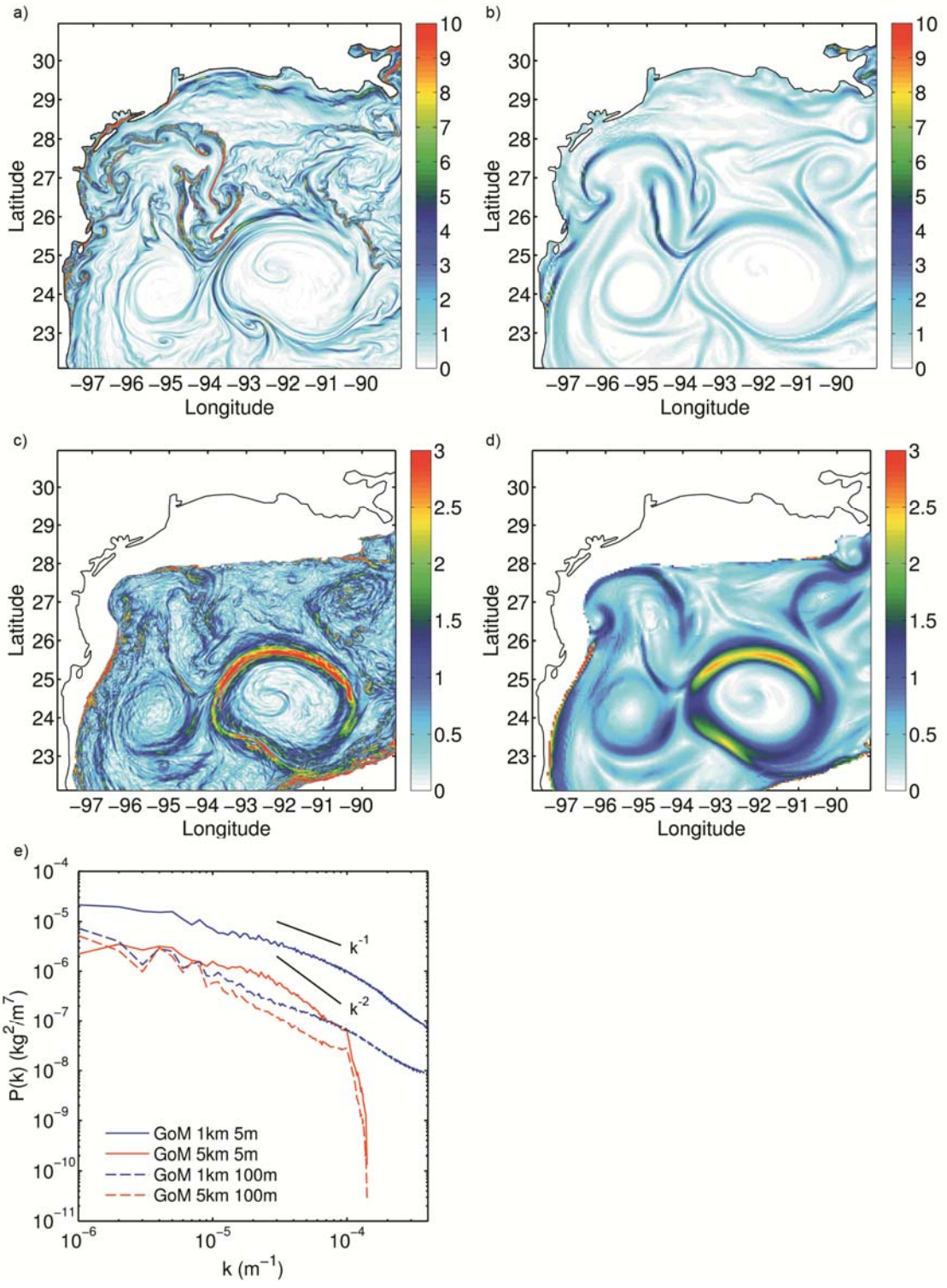
a)
b)
c)
d)
e)
Latitude
Longitude
−97 −96 −95 −94 −93 −92 −91 −90
23 24 25 26 27 28 29 30
0 1 2 3 4 5 6 7 8 9 10
0 0.5 1 1.5 2 2.5 3
P(k) (kg²/m⁷)
k (m⁻¹)
10⁻⁴ 10⁻⁵ 10⁻⁶ 10⁻⁷ 10⁻⁸ 10⁻⁹ 10⁻¹⁰ 10⁻¹¹
10⁻⁶ 10⁻⁵ 10⁻⁴
k⁻¹
k⁻²
GoM 1km 5m
GoM 5km 5m
GoM 1km 100m
GoM 5km 100m

Figure 3.8: Instantaneous pattern of $\left|\nabla_h \rho\right|$ at 5 m (top panels) and 100 m (middle panels) of 1 km (a and c) and 5 km (b and d) runs on April 21, 2005 (Unit: 10^{-5} kg m^{-4}), and their azimuthally-integrated power spectra (e).

We further quantify changes in the w representation by plotting the root-mean-square (RMS) fluctuation (standard deviation) of the instantaneous vertical velocity at the two resolutions, calculated over regions where the water column is deeper than 750 m and using instantaneous snapshots saved every hour during the 40 days of the Lagrangian deployment (Figure 3.9a). An increase in standard deviation by two to three folds is found in the nested run compared to the parent simulation at all depths. Below 500 m depth, the standard deviation of w in LR remains approximately constant until 2,700 m, and then decreases as more and more grid points are found in the model bottom layer, where w converges to zero; in HR, on the other hand, the standard deviation grows with depth until it reaches its maximum at approximately 2,700 m depth, and then decreases. The deep vertical velocity maximum is due to dispersion of the first few baroclinic models and to a resonance mechanism that affects mainly the first baroclinic mode whenever small scale vorticity structures are resolved (Danioux et al., 2008). In a subsequent paper Danioux et al. (2011) showed that the average duration of the wind events influences how many baroclinc modes disperse into the deep layer, and consequently the depth of the maximum.

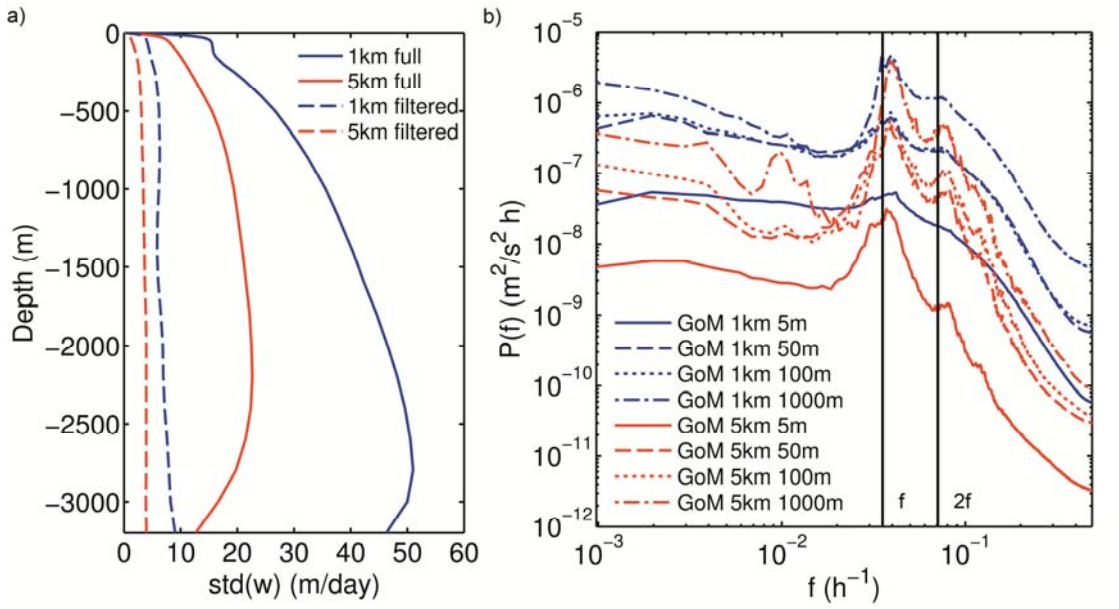

Figure 3.9: Panel (a): Domain-averaged vertical profile of the root-mean-square fluctuation of instantaneous vertical velocities (solid lines) and of their low-pass filtered counterpart with the cut-off frequency 0.8*f* (Unit: m/day). Panel (b): frequency power spectra of vertical velocities at 5, 50, 100 and 1000 m. (Unit: m^2/s^2 h). In both figures only regions where the water column is deeper than 750 m have been considered.

To prove that the deep maximum and most of the w variance are linked to near inertial waves we reconstructed w filtering out all frequencies greater than 0.8f, where f is the inertial frequency ($f \sim 0.035$ h^{-1} in our domain). The reconstructed velocities for LR and HR display a similar behavior with depth, the HR deep maximum is absent, and the standard deviation is greatly reduced in both runs.

As expected from the analysis of the standard deviation, the vertical velocity frequency spectra (Figure 3.9b) show two peaks, the amplitude of which increases with depth. The first peak is around the inertial frequency f and the second is at twice its value,

again in agreement with Danioux et al. (2008, 2011) and Koszalka et al. (2009). Higher velocities in HR within and immediately below the mixed layer reflect the contribution of all frequencies, with the sub-inertial increasing the most, while at depth the increase at low frequencies is of small amplitude.

The vertical velocity distributions in HR and LR are similar in shape throughout the water column (Figure 3.10 shows the PDFs of w at 50 m depth), are non-Gaussian, have very different standard deviations at all depths, as quantified in Figure 3.9a, and are symmetric around zero everywhere but close to the surface, where they are slightly skewed toward negative values. This is in agreement with previous findings for an idealized eddy-dominated flow (Koszalka et al., 2009), and for frontal regions (Mahadevan, 2006; Capet et al., 2008c).

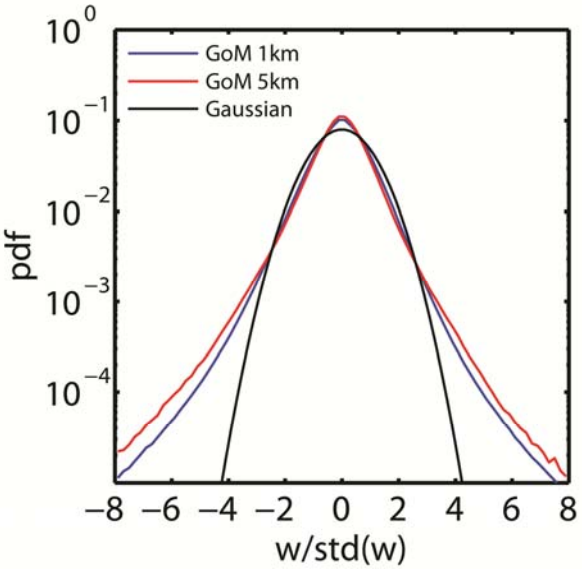

Figure 3.10: Probability density function of Eulerian vertical velocities at 50 m, normalized to have unit variance, compared to a Gaussian distribution.

One question that arises from the analysis of the vertical velocities is the realism of the model representation of w, given that the instantaneous values are one order of magnitude greater than that predicted by theoretical models applied to eddy-dominated flows (e.g. Pinot et al., 1996; Shearman, et al., 1999; Martin and Richards, 2001). Within the mixed layer, vertical velocities as high, —and higher than here—, have been found in observations or in models in presence of frontal instabilities due to strong ageostrophic submesoscale circulations (e.g. Thomas et al., 2008; Klein and Lapeyre, 2009; Molemaker et al., 2010; D'Asaro et al., 2011). In HR, ageostrophic circulations occupy mostly the mixed layer between the large Loop Current eddies, and their peripheries (Figure 3.1). In the upper 20 - 30 m, those ageostrophic motions, not fully resolved at 5 km, are also responsible for the appearance of horizontal divergence and convergence regions observed in the northwestern Gulf of Mexico in satellite images of *Sargassum* distributions (Gower and King, 2008; Zhong et al., 2012). ROMS can therefore simulate the observed patterns of surface tracers only if the vertical velocities in the mixed layer are as intense and highly variable in both space and time as in HR.

Below the mixed layer, differences in the vertical velocities between the two resolutions are (mainly) linked to the energetic near-inertial field associated with the eddies, comprising both the Rings and smaller cyclones and anticyclones. As shown earlier, it is not possible to infer the reliability of the model representation of the instantaneous w field from temperature or salinity profiles, as the differences in w do not impact much the water column stratification. The model we use is hydrostatic and within such approximation physical dispersion of internal waves due to non-hydrostasy is not represented, potentially causing an overestimation of the vertical velocity field (Vitousek

and Fringer, 2011). Such tendency is counterbalanced by numerical dispersion that mimics the missing physical dispersion due to nonhydrostatic effects. The internal wave field representation, however, may be affected by such numerical dispersion in unrealistic ways. Vitousek and Fringer (2011) have shown that this is especially true in the case of solitary waves. Therefore, nonlinearity and non-hydrostasy cannot be neglected near continental shelves and ocean ridges where solitary-like wave train can develop more easily (Scotti and Pineda, 2004). In deep waters and over moderate topography, on the other hand, oceanic internal waves are nearly hydrostatic (Kantha and Clayson, 2000) and well represented by ROMS (Vitousek and Fringer, 2011). Here we found that differences in the instantaneous vertical velocity representation between HR and LR at depth are mainly associated with the near-inertial wave field that develops in and around the eddies, in deep waters and over smoothly varying topography, where we focus our analyses. Additionally, while observations of w in deep waters and within eddies are extremely rare, one of the best examples is from the central Gulf of Mexico. Rivas et al. (2008) used sixteen months of observations (May 2003–August 2004) from a surface-to-bottom mooring equipped with two upward-looking 75-kHz Teledyne RDI acoustic Doppler current profilers (ADCPs) located at depths of 361 m and 1227 m to calculate vertical velocities and heat flux exchanges. They found evidence of coherent signals of instantaneous vertical velocities below the mixed layer around 170–250 m/d in association with the passage of three Loop Current eddies. The vertical velocity measurements showed high-frequency variability on periods less than 2 days, attributed by the authors to the presence of tides and internal waves. Even larger w values have

been measured in the Algerian Sea, at depths between 1900 and 2400 m, during the transit of large anticyclones by van Haren et al. (2006).

In our model, we found the highest values of w in the central portion of our domain, where the mesoscale eddy field dominates the dynamics, for increasing resolution. Despite possible biases associated with the use of a hydrostatic model, our results indicate that by increasing the horizontal resolution of ROMS we achieved a more realistic representation of the submesoscale field that develops in and around eddies.

3.4 The Lagrangian Trajectories

Before quantifying the impact of horizontal resolution on the representation of particle dispersion, we take an overview of the global distribution of the particles. We shall also illustrate the effect of vertical particle motion on their horizontal distribution by comparing the isobaric (2-D) particle trajectories, to the 3-D particle experiments, at the two resolutions.

Figure 3.11 shows the horizontal distribution of 2-D particles released at depth of 5 m and 100 m, 40 days after deployment. Their positions are superposed on the vorticity field in both HR and LR integrations. The isobaric particles tend to align themselves to form extensive lines and spiral structures around eddies, with length scale up to O(100km). At 5 km resolution, those lines are reminiscent of transport along unstable manifolds in chaotic two-dimensional flows (see e.g. Tél et al., 2000). At 1 km resolution, on the other hand, near surface particles found in regions of elevated submesoscale activity display more disordered patterns. Those patterns are comparable to those revealed by the high-resolution ocean color satellite images of surface *Sargassum*

(Gower and King, 2008). Zhong et al. (2012) demonstrated that they are linked to the strong horizontal convergence and divergence field generated by ageostrophic processes within submesoscale range responsible for large $\frac{\partial w}{\partial z}$ close to the ocean surface, as also noticed in surface reflectance images (McWilliams et al., 2009). At 100 m, on the other hand, the aggregation process is weaker due to the weakened horizontal convergence field.

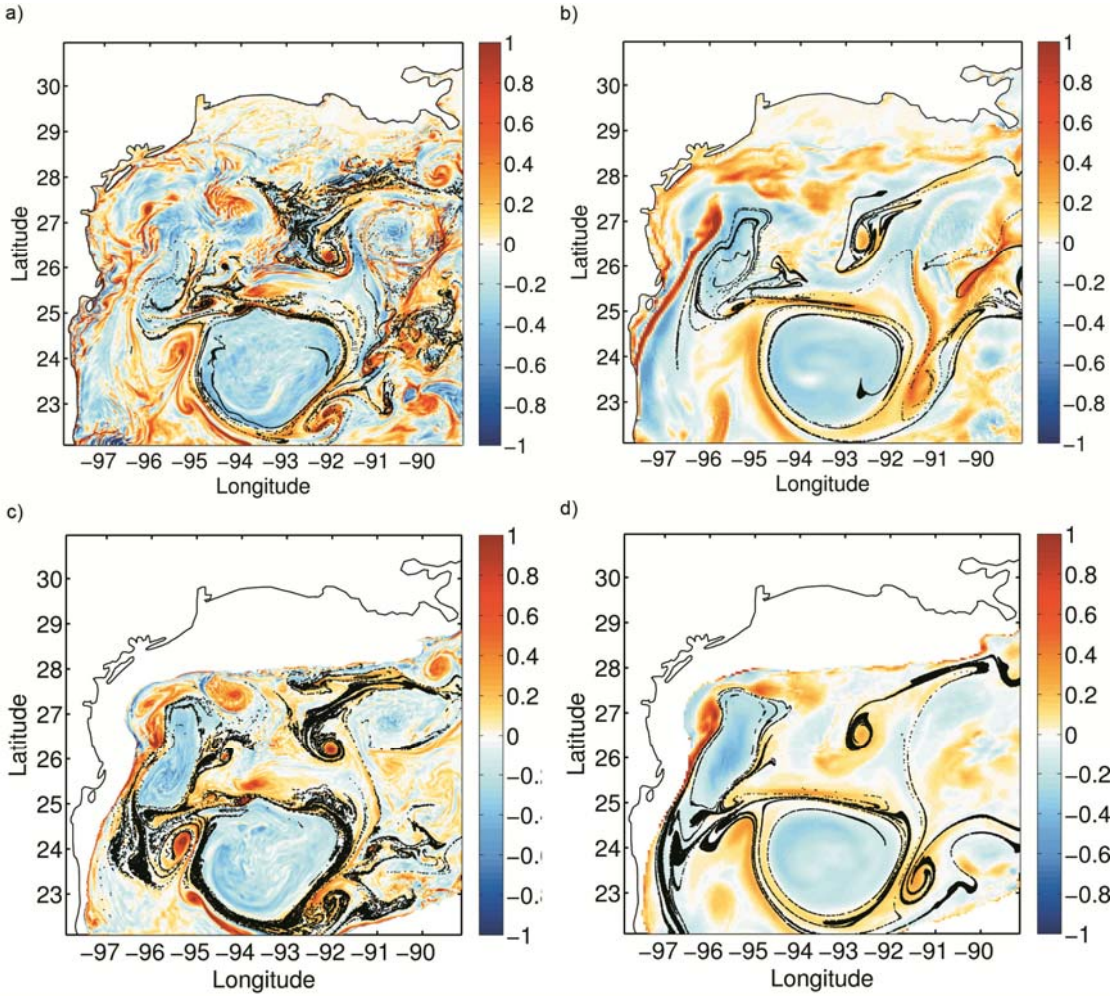

Figure 3.11: Distribution of isobaric (2-D) particles superposed on the relative vorticity field normalized by the Coriolis frequency f at 5 m (top panels) and 100 m (bottom panels) 40 days after deployment. (a-c) 1 km resolution and (b-d) 5 km resolution integrations.

In Figure 3.12 we present the depth distribution of the 3-D tracers released at 5 m and 100 m, again after 40 days. 3-D particles deployed close to the surface, mapped onto the horizontal plane, are distributed in patterns closely resembling those of the isobaric

tracers but more diffuse and widespread. This is because close to the surface the submesocale convergence and divergence zones modify the particles patterns, and once the particles move to different depths they are carried by horizontal flows with slightly different spreading rates. For particles deployed below the mixed layer, the positions after 40 days mapped onto the horizontal plane are very similar. The spreading across the lines resembling unstable manifolds is evident at 1 km, but still more diffuse than in LR. The vertical displacement around the mesoscale structures, on the other hand, remains significantly greater in HR than in LR at all depths as quantified by the PDFs in Figure 3.13. Due to the surface boundary constraint and deployment depths, particle displacements measure a net downward flux. Consistent with the horizontal distribution maps, a fair number of particles released close to the surface reach depths greater than 100 m in HR, while approximately half of this distance is covered by particles deployed in the LR run. In particular, after ten days all particles in LR can be found within the mixed layer, while more than 25% of the particles in HR are located below it. Differences are also pronounced for tracers released at 100 m depth, due to stronger upwelling and downwelling vertical velocities in HR than LR, enhanced at the edge of the Loop Current eddies. In LR particles released at 100 m remain below the mixed layer at all times, while in HR approximately 10% of the tracers are found in the mixed layer already after 10 days, with important consequences for the representation of biological or chemical vertical exchanges in ocean models. Independently of depth, the difference in the simulated particle displacement in the two runs grows over the first few days and stabilizes after day 10 for particles deployed close to the surface, and after about a week for particles released at 100 m, as later quantified by the dispersion curves. Movies

showing the evolution of the particle depth distribution for all 3-D deployments at 1 km and 5 km resolution are available as Supporting Material.

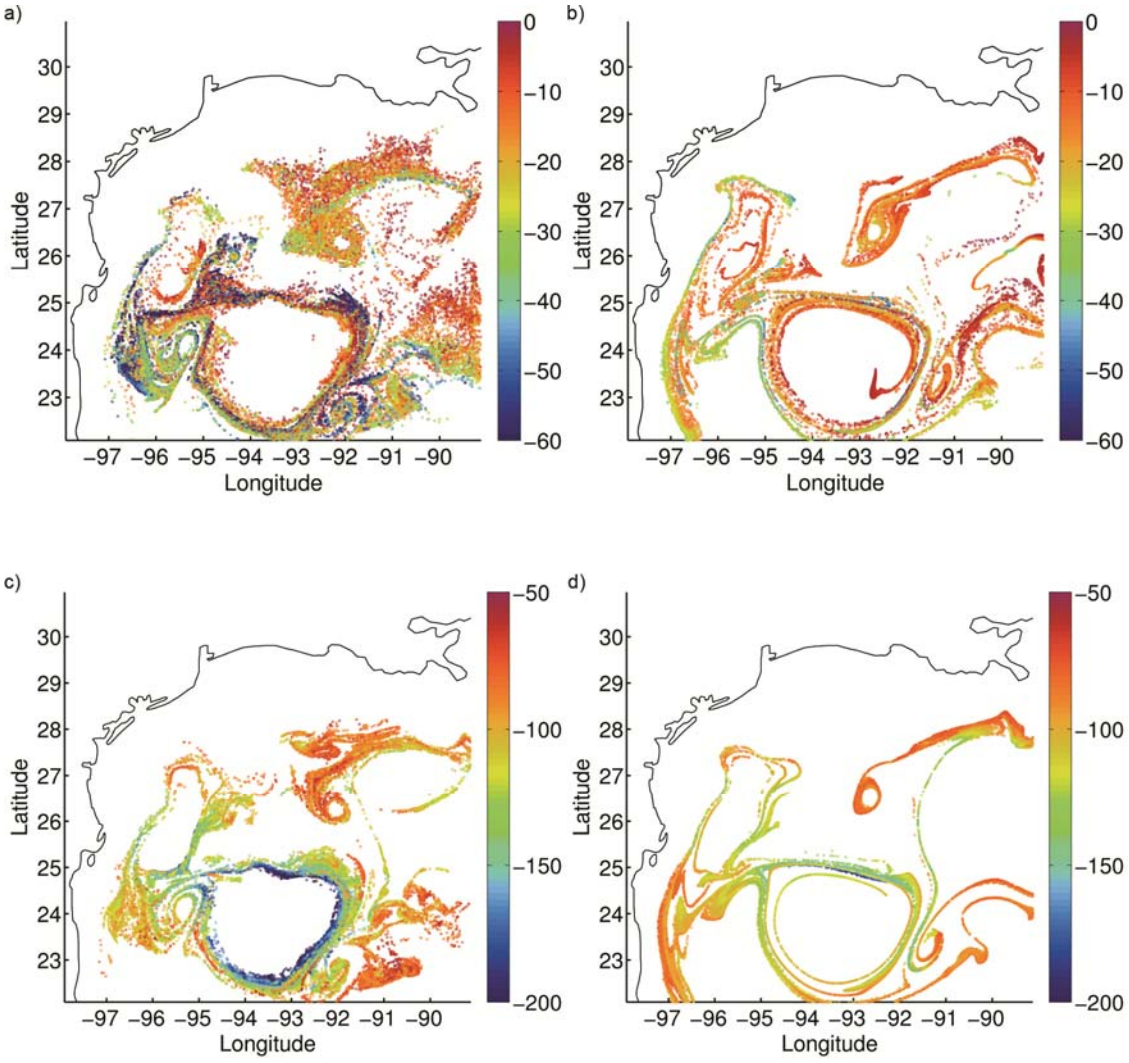

Figure 3.12: Vertical distribution of 3-D particles 40 days after deployment. The color of the particles indicates their depth (Unit: m). (a) and (b): Tracers initially released at 5 m in the 1 km and 5 km horizontal resolution runs, respectively. (c) and (d): Tracers initially released at 100 m in the 1 km and 5 km resolution integrations.

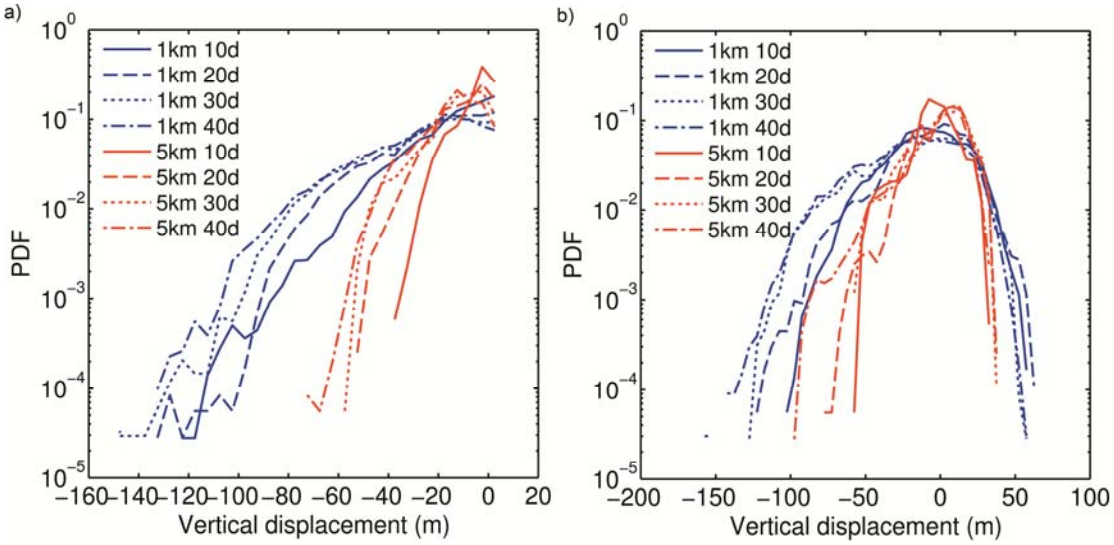

Figure 3.13: Probability density function (PDF) of the vertical displacement of 3-D particles 10, 20, 30, and 40 days after deployment in the nested (blue curves) and parent (red curves) simulations. (a): PDF for particles deployed at 5 m; (b): PDF for particles deployed at 100 m.

Finally, it is worth noticing that the tracer velocity distributions are analogous to those of the Eulerian fields. 2-D particles display u and v PDFs that are statistically indistinguishable from the Eulerian ones at 5 m. The u, v and w PDFs of 3-D tracers, grouped between tracers found at any time above or below 25 m depth, compare very well with the Eulerian distributions close to the surface or at 50 m (not shown). The Lagrangian particles, while non-uniformly distributed, are nonetheless mapping velocities that are representative of the whole domain of integration in regions away from the continental shelf and from the core of the larger eddies (concentrations of particles on the continental shelf and inside the Rings are very low at all times).

3.5 Horizontal and Vertical Lagrangian Transport

To further evaluate the transport properties in the integrations considered, we compare the absolute dispersion, horizontal and vertical, for the Lagrangian tracers released in the Gulf of Mexico.

Horizontal Lagrangian dispersion at the ocean mesoscales (10–500 km) has been extensively studied for several decades theoretically, experimentally and numerically. Its time evolution is determined by mesoscale motions, which are identically captured at both resolutions in our runs. As shown by Taylor (1921), at short time scales (shorter than Lagrangian autocorrelation time), particles passively advected in turbulent flows have memory of their initial conditions, and absolute dispersion follows a ballistic regime (i.e. $A^2(t) = 2Kt^2$). In contrast, at times much longer than the Lagrangian autocorrelation time, the absolute dispersion in Gaussian, homogeneously and stationary flows is diffusive or Brownian (i.e. $A^2(t) = 2Et$). Theoretical work developed in the framework of two-dimensional (2-D) turbulence flows has been extended, with numerical studies, to account for the presence of coherent vortices (Babiano et al., 1987; Provenzale, 1999; Pasquero et al., 2001). The impermeability of coherent vortices to inward and outward particle fluxes, and the presence of energetic circulation cells surrounding the vortices have been associated to anomalous dispersion regimes found at times comprised between the Lagrangian integral time and the appearance of Brownian scaling (Elhmaidi et al., 1993). The analysis of horizontal dispersion in baroclinic (Berloff et al., 2002; Bracco et al., 2004), stably stratified (van Aartrijk and Clercx, 2010), and Boussinesq flows (Koszalka et al., 2009; Ohlmann and Mitarai, 2010; Drake et al., 2011) characterized by

the presence of coherent vortices has confirmed the existence of anomalous dispersion regimes. In the ocean, surface drifters and subsurface floats have been used to quantify absolute dispersion in various basins (de Verdiere, 1983; Osborne et al., 1989; Sanderson and Booth, 1991; Rupolo et al., 1996; Falco et al., 2000; Bauer et al., 2002; LaCasce, 2008; Berti et al., 2011), including the Gulf of Mexico with the ongoing GLAD experiment (www.carthe.org/glad). An anomalous scaling approximately proportional to $\sim t^{3/2}$ has been found in very diverse environments, ranging from the Kuroshio Extension (Osborne et al., 1989), to the Northeast Atlantic (Sanderson and Booth, 1991). In all those cases, however, the presence of large-scale inhomogeneities makes the attribution of the anomalous dispersion to eddies uncertain. More recently, numerically simulated isobaric Lagrangian particles, and floats and drifter data have been fruitfully used in applications ranging from the diagnosis of oil spreading (Mariano et al., 2011; North et al., 2011; Dietrich et al., 2012), to the investigation of egg and larval distributions (Siegel et al., 2003; Sundelöf and Jonsson, 2012). In those last studies, the transport at times and lengths typical of submesoscale processes may be potentially important, but has not been addressed.

To quantify how different scales impact the tracer spreading, we then calculate the finite size Lyapunov exponents (FSLE), which provide a direct measure of the local stirring of the flow (Artale et al., 1997) by generalizing of the concept of Lyapunov exponent to finite separations of size δ**.** FSLE have been shown to be able to separate mesoscale from submesoscale stirring in the ocean (d'Ovidio et al., 2009; Haza et al., 2012; Schroeder et al., 2011, 2012), and provide an alternative measure to two-particle dispersion for non-homogeneous flows in closed basins.

Finally, we present a vertical dispersion analysis. Vertical dispersion in geophysical flows is far less studied than the horizontal counterpart, and no experiments ever tested the validity of theoretical arguments in the ocean. A diffusive regime is expected at short times; at longer times, a few recent papers have found that in idealized, stably stratified, non-rotating turbulence systems, stratification arrests single particle dispersion in the direction of stratification, so that the Brownian regime is never attained (Kimura and Herring, 1996; van Aartrijk et al., 2008; van Aartrijk and Clercx, 2010).

In the following calculations, particles transported to the continental slope in waters shallower than 750 m are excluded (the trajectories excluded represent less than 10% of the total, independently of depth).

3.5.1 Horizontal Dispersion and Finite Size Laypunov Exponents

Horizontal dispersion, $A^2(t)$, describes the time evolution of the horizontal square distance traveled by each particle, averaged over all particles. It is defined as $A^2(t) = \left\langle \left[\mathbf{x}_i(t) - \mathbf{x}_i(t_0) \right]^2 \right\rangle$, where $\mathbf{x}_i(t) = \left(x_i(t), y_i(t) \right)$ is the i-th particle horizontal position at time t, and t_0 is the deployment time.

Figure 3.14 shows the horizontal absolute dispersion for 3-D particles initially deployed at 5, 50 and 100 m depth. Curves in the meridional and zonal directions are plotted separately. The representation of horizontal dispersion is independent of resolution. The curves in the HR case at most display slightly larger dispersions at short times (no more than a couple of days), indicating, as expected, that resolving the submesoscales has little impact on the averaged horizontal transport. The magnitude of the dispersion immediately after deployment is slightly smaller for particles released

below the mixed layer (100 m), compared to the ones close to the surface or at the base of the mixed layer (5 and 50 m). In all cases, the initial dispersion is ballistic during the first two days in the meridional direction and for less than one day in the zonal component. The meridional dispersion is larger than the zonal and then flattens, due to the trapping of a large number of particles into the periphery of a large Loop Current eddy (the one in the southern portion of the domain in Figure 3.1) that is slowly rotating towards the east. Those trapped particles begin moving southward around Day 10, causing an increase in meridional dispersion at the expenses of the zonal component. After Day 20, due to the continuous entrainment of particles around the eddy, both zonal and meridional dispersion curves flatten, given that the center of mass of the Ring moves westward at a speed much smaller than its turnover velocity, approximating the behavior of a frozen vortex (Babiano et al., 1987). In Figure 3.14a and c, we also plot the absolute dispersion of the isobaric particles deployed close to the surface and at 100 m. For both HR and LR runs the curves are very close to the ones found for 3-D tracers, despite the differences in the horizontal distribution of the particles (Figure 3.11), demonstrating that the ensemble averaged transport is non-locally controlled by the mesoscale flow. From this analysis we can conclude that the influence of resolving the submesoscales on the transport of Lagrangian tracers is limited to the different pattern formation.

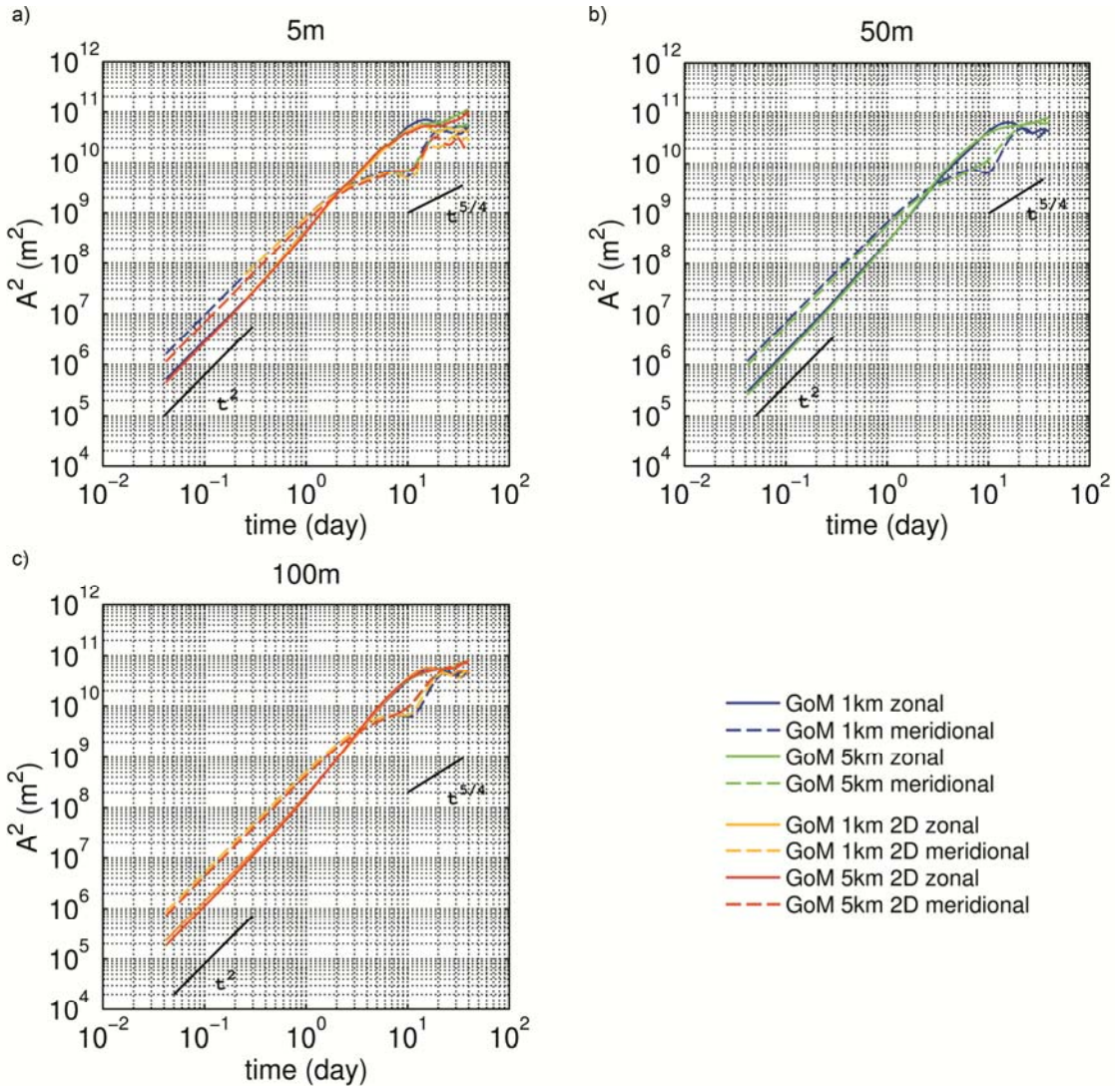

Figure 3.14: Horizontal absolute dispersion of 3-D particles initially released at (a) 5 m, (b) 50 m, and (c) 100 m depth. In (a) and (c) dispersion curves of isobaric (2-D) particles are also plotted.

The FSLE (Figure 3.15), calculated following the fastest-crossing method (Poje et al., 2010) and using the isobaric tracers, are characterized at large separation scales (δ >

100 km) by a slope proportional to δ^{-1}, indicative of a ballistic regime in the two-particle relative dispersion in all cases (5 m, 100 m, HR and LR). For separation scales smaller than 100 km the FSLE curves in LR and at 100 m in HR are almost flat, and indicative of (mainly) non-local spreading governed by the presence of mesoscale coherent eddies larger than the separation distance. Such behavior corresponds to an approximate k^{-3} slope in the velocity spectra. At 5 m depth in the high resolution run, the strong submesoscale processes near the surface dominate the energy contained between 10 km and 100 km (see Figure 3.3), and induce local spreading (i.e. the spreading at a given separation is governed by processes at that same scale) as quantified by the slope ($\delta^{-0.6}$) in the FSLE curve, which corresponds to a Richardson's-like relative dispersion. For separation distances below 10 km, the FSLE curve for surface tracers in the HR case continues to grow, consistent with previous modeling studies, but with a slope not as steep as measured by surface drifters (Haza et al., 2012; Schroeder et al., 2011; unpublished CARTHE results for the west Gulf of Mexico), suggesting that the model resolution is not yet sufficient to reproduce all dynamics relevant at those scales.

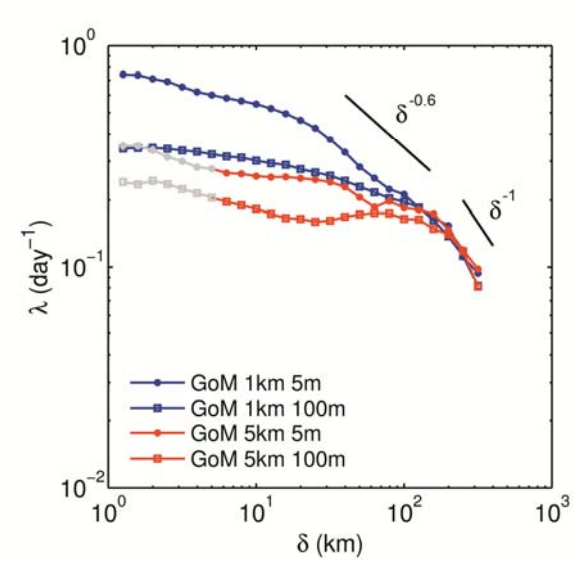

Figure 3.15: Finite size Lyaponov exponents of 2-D particles at 5 m and 100 m depths in the nested (blue curves) and parent (red curves) simulations. Particles are deployed at a minimum distance of 1 km in both runs. The gray portions of the red curves indicate displacements below the model grid scale.

3.5.2 Vertical Dispersion

The vertical dispersion of ocean tracers has not been studied to our knowledge. Floats and drifters are confined to isobaric surfaces or fixed depth, and numerical models represent the only tool for a systematic dispersion analysis, but validation of numerical results is not possible in practice. Direct numerical simulations of vertical particle transport in 3-D forced, stratified (non-rotating) turbulent flows have been recently performed (van Aartrijk et al., 2008; van Aartrijk and Clercx, 2010). In the vertical direction, the authors identify three regimes: the classical ballistic t^2, a plateau that scales as the buoyancy frequency N^{-2}, and a diffusive or subdiffusive limit, depending on

stratification, for times much longer than the Lagrangian decorrelation. In all their simulations, the flow is turbulent but coherent eddies are not present, due to the absence of rotation.

Vertical dispersion is simply calculated using our 3-D tracers as $A_z^2 = \left\langle \left[z(t) - z(t_0) \right]^2 \right\rangle$, and it is shown for the two integrations in Figure 3.16. At first glance, it is evident that horizontal model resolution plays a fundamental role in the representation of vertical transport. High-resolution results are characterized by significantly larger vertical dispersions than the LR counterparts at all depths, due to the more energetic vertical velocity field. In agreement with Taylor's theory (1921), and with the stratified turbulence numerical experiments (van Aartrijk et al., 2008), the vertical dispersion curves follow a ballistic regime for very short times (a day at most). During the ballistic time, differences between HR and LR are larger close to the surface and decrease with depth, in agreement with the relative increase in super-inertial energy seen in the frequency spectra at various depth. Also, the dispersion is greater at the base of the mixed layer or below it than at the surface, due to the weak vertical velocities in the first few meters of the water column (see Figure 3.9a). In the case of particles deployed closed to the ocean surface, the HR and LR curves at intermediate times diverge even further reaching differences over an order of magnitude. This is due to the large vertical velocities found inside the submesoscale vorticity filaments resolved only by HR. From 10–15 days to the end of the integration, independent of resolution, particles are subject to a slightly subdiffusive regime, with $A_z^2(t) \sim t^{0.75\pm0.1}$. In the case of particles deployed at 50 m and 100 m, the differences between HR and LR is reduced after Day 1. On this time scale, the dispersion difference at depth is governed, predominantly by the intensification

of the near inertial wave motions in HR compared to LR, with alternating positive and negative displacements of the particles. At times larger than the inertial scale, the higher velocities around the periphery of the eddies in HR are responsible for maintaining larger dispersions. At both resolutions, the onset of the plateau found by van Aartrijk et al. (2008) is visible for particles from Day 10 onward. The integration time is too short to allow for a diffusive or subdiffusive regime to be identified at depth. At intermediate times, all vertical dispersion curves are not as smooth as the horizontal ones. This is likely due to the fact that vertical velocities are highly inhomogeneous throughout the (upper) water column, and more so in the HR case.

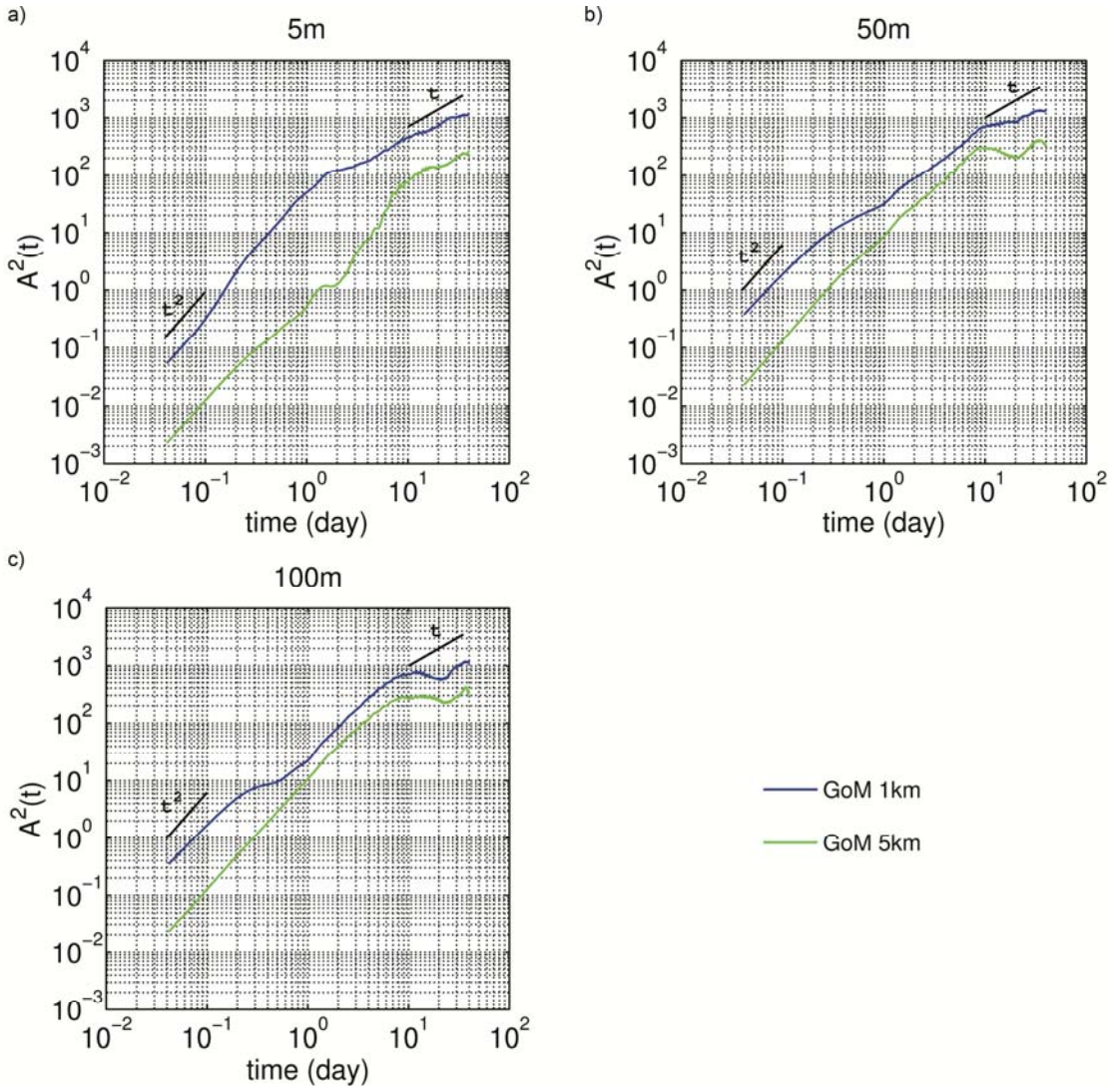

Figure 3.16: Vertical absolute dispersion of 3-D particles initially released at (a) 5 m, (b) 50 m, and (c) 100 m depth.

Overall, the modeled vertical Lagrangian transport in the upper 200 m is strongly enhanced by increasing horizontal resolution. Such increase is larger close to the surface, where submesoscale ageostrophic dynamics contribute to the formation of strong

convergence and divergence patterns and strong vertical accelerations (Zhong et al., 2012), but it is not negligible (5–6 times in our simulations) also below the mixed layer, at least on time scales comparable with the Eulerian time of the flow.

3.6 Conclusion and Discussion

In this study, we numerically investigated how varying the horizontal resolution from 5 km to 1 km impacts the representation of horizontal and vertical transport in a regional ocean model. Our area of interest is the northwestern Gulf of Mexico, where Loop Current eddies are a major source of mesoscale variability in the upper 1,000 m of the water column, and large scale frontal structures are absent.

Energetic submesoscale filaments and a population of small vortices emerge when the model horizontal resolution is increased. As a result, in the 1 km integration the horizontal energy power spectra at all depths are slightly flatter than in the lower resolution case, and at the surface the slope in the direct cascade range approaches k^{-2}. The amplitude of the horizontal eddy kinetic energy, the overall stratification and the horizontal velocity distributions, however, are barely affected by the model resolution. We further quantified how resolving the submesoscale processes impacts the overall transport by releasing a large amount of Lagrangian tracers in an area of high submesoscale activity away from the continental shelf and outside the Loop Current eddies. The horizontal dispersion curves for isobaric tracers deployed close to the ocean surface and at 100 m, and for neutrally buoyant Lagrangian particles released at 5 m, at the base of the mixed layer, and at 100 m depth, are indistinguishable in the two integrations at all times. The space-averaged transport is driven by the (almost identical)

mesoscale flow, with the Loop Current eddies stirring the tracers around their periphery. This is verified for the isobaric particles despite significant differences in the details of the horizontal Lagrangian patterns simulated. The strong divergence and convergence zones generated by the ageostrophic processes close to the ocean surface that are resolved only at 1 km resolution are indeed responsible for the creation of areas where particles accumulates (Zhong et al., 2012), and for the difference in the FSLE for small displacements. The contribution of submesoscale processes is therefore "limited" to the details of the tracer distributions around the mesoscale pathways, but those details important for biological or chemical applications, as recently experienced in the aftermath of the Deepwater Horizon oil spill.

In contrast, the amplitude of the modeled vertical velocities increases significantly with increasing horizontal resolution through the whole water column. In our simulations, vertical velocity distributions do not change in shape, but are resolution dependent in their variance. The representation of the energy content is affected by the horizontal resolution at all frequencies. In the 1 km resolution case, large vertical velocities are found not only in correspondence to surface intensified submesoscale vorticity filaments and in straining regions at the edge of the eddies, but also inside the eddies. Indeed, below the mixed layer the velocity field intensifies particularly inside the Loop Current eddies, where the instantaneous values of the modeled vertical velocity can reach several tens of m/day (up to 80 m/day) in the 1 km resolution run. Even higher values have been found in moored ADCP measurements in correspondence with the passage of Rings in the central portion of the Gulf of Mexico, suggesting that the model w intensity may further increase at higher resolutions than considered here.

The modeled vertical dispersion of neutrally buoyant Lagrangian tracers also increases with horizontal resolution. Near the surface, we find that the increase in dispersion is over an order of magnitude for the first ten days past deployment, and decreases slightly afterwards. At the base of the mixed layer and at 100 m the increase reduces to approximately five folds past the ballistic regime, i.e. one day after deployment. This conspicuous difference highlights the crucial role of ocean submesoscale processes in the vertical exchange of tracers. In presence of an energetic eddy field that extends through the water column, as in the case of the Gulf of Mexico, processes at O(1) km scales are important not only in the upper ocean (Mahadevan and Tandon, 2006; Capet et al., 2008a; Klein and Lapeyre, 2009; Lévy et al., 2012), but also at depth. In this work, this is verified on times at least comparable to the Eulerian time scale of the flow.

Finally, we remark that resolving submesoscale motions at depth where mesoscale eddies are abundant may, in principle, require high resolution in both horizontal and vertical directions (Capet et al., 2008a; Klein et al., 2008). In our runs, the first 150 m of the water column are well resolved vertically, and we concentrated our Lagrangian analysis to those depths, limiting the attention to areas with no steep topographic features. We examined the influence of the vertical resolution on the model representation of transport processes by performing two (shorter) auxiliary runs with ROMS configured with twice as many vertical layers. Differences in both vertical velocity fields and vertical dispersion curves when using 60 or 30 layers were negligible on a time scale of 20 days, but longer integrations are needed to determine the role of vertical resolution.

CHAPTER 4

CONCLUSIONS AND FUTURE WORK

4.1 Conclusions

This thesis examined the role of submesoscale dynamics on the tracer transport and dispersion in an eddy-dominated flow. The two major conclusions are drawn as below, in response to the scientific questions raised in Chapter 1:

1. Strong submesoscale processes can regulate the surface tracer distribution and form characteristic heterogeneous pattern with scales up to tens of thousands meters. In the Gulf of Mexico, the westward-propagating Loop Current Eddy is large, long-lived and energetic. It strongly stirs the ambient fluid and the high strain along the periphery of the eddy induces plenty of narrow and elongated submesoscale filaments, which are usually associated with enhanced vertical velocities. Due to the surface boundary restriction, the vertical velocity gradient can be very high near the surface and therefore strong surface convergence/divergence zones emerge. This unique surface characteristic facilitates the aggregation of the surface tracers and is responsible for the pattern formation of the floating materials at the meso- and submesoscales.
2. The submesoscale impact on the ocean transport is quite different in the horizontal and vertical components. When the model resolution increases, a large amount of submesoscale structures such as eddies, fronts and filaments emerge and an accelerated forward KE cascade can be identified. However, the overall

stratification and the horizontal velocity PDF are almost unaltered. From the Lagrangian viewpoint, the particle distribution at the surface show more detailed structures due to resolving more small dynamics, but the horizontal transport measured by the absolute dispersion is independent of the resolution. In contrast, the modeled vertical velocity increases significantly throughout the whole water column and the vertical dispersion is of one order larger than that in the lower resolution model. It therefore suggests that the impact of the submesoscale processes on the ocean transport is very anisotropic, and primarily on the vertical direction.

Besides the major conclusions, several additional remarks are also notable and may be relevant to the other studies.

1. The Lagrangian particle surface distribution in our model is different from that in the 2-D or QG turbulence. Previous studies have shown that the behavior of the particles in the 2-D and QG turbulence depends on where they are initially located. There is no aggregation phenomenon in those turbulences since they are inherently divergence-free. It is well known that the mesoscale eddies in the ocean can maintain the source water properties for their life time. This study indicates that the property distribution inside the eddy is not homogeneous as predicted by the QG theory but more complex.
2. The maximum vertical velocity is observed in the deep layer, which can be attributed to the near inertial motions associated with the presence of mesoscale eddies as shown in previous studies. The near inertial motions are the main mechanism that can transfer the atmospheric kinetic energy into the deep ocean.

By increasing the model resolution, the vertical velocity increases at all depths but the maximum occurs in the deep layer, suggesting that smaller scale dynamics enhance the downward energy propagation. This result is consistent with the theoretical simulation in Danioux et al. (2011). However, it is still difficult to determine how much the contribution of submesoscale processes is in this propagation mechanism.

3. The absolute dispersion in the vertical is a measure that is not commonly used compared to its horizontal counterpart. But it is a very useful tool to quantify the vertical transport and potentially the vertical diffusivity. In this study, the vertical dispersion in a realistic simulation is presented and some dispersion features can be compared with the previous study in the 3-D stratified turbulence model. The initial particle behavior follows a ballistic law in both models. Due to the stratification, the plateau is also visible in the intermediate time. In the long run, a subdiffusive regime is identified in our model instead of a diffusive regime in the 3-D stratified turbulence. This may be attributed to the local dynamics such as strong mesoscale eddies.

Overall, this study emphasizes the important role of strong vertical velocity due to the development of the ageostrophic circulation associated with the submesoscale processes in affecting the ocean tracer distribution and transport properties. The strong ageostrophy differentiates the submesoscale dynamics from the meso- and large dynamics and therefore the submesoscale processes make an unique contribution on the tracer behavior in the ocean.

4.2 Future work

The above research on the submesoscale dynamics provides a good physical base for understanding the ocean tracer distribution and transport, which could be instrumental in studying the surface pollutant dispersion such as spilled oil and biological vertical nutrient replenishment. Besides the transport process, ocean mixing is another important process that affects the physical and biological properties in the ocean. The mixing processes span a wide range of spatial and temporal scales. A large volume of previous studies have concentrated on the mixing on mesoscale or larger. Submesoscale mixing processes, however, are still not well explored since they are very difficult to measure. Presently there is no good parameterization of submesoscale mixing processes in the numerical models though its significance in simulating and predicting ocean circulation and climate change has been well recognized. General ocean circulation model and climate model usually can only resolve a few tens of kilometers due to the limitation of computer power. The submesoscale processes in such models are usually treated as subgrid processes using Fickian diffusion parameterization with an eddy diffusivity much larger than molecular diffusivity for tracer equation. This simple parameterization cannot accurately reflect the physical characteristics of submesoscale dynamics. The constant (or slightly varying) eddy diffusivity is corresponding to a Brownian absolute dispersion regime in the Lagrangian framework which can be only observed at times much longer than Lagrangian autocorrelation time scale. In the typical submesoscale range (O(1 day)), the dispersion is anomalous and non-Fickian. Recent observations of Lagrangian drifters released in the submesoscale range have indicated that the pair-particle dispersion is much faster than that predicted in numerical model (e.g. Schroeder et al, 2012). The physical mechanism to interpret this enhanced mixing is still an open question and only a

few works using stochastic modeling have been done in its parameterization. To approach these problems, it is important to determine what dynamical processes and how they could potentially affect the submesoscale mixing. The submesoscale instabilities and/or mesoscale strainings, etc. could be such key players in controlling the isopycnal and diapycnal mixing at the submesoscale range. Further study still needs numerical simulation as the major tool in exploring the mechanisms, but advanced technology in observing submesoscale processes would provide a realistic gauge for the numerical results.

REFERENCES

Artale, V., G. Boffetta, A. Celani, M. Cencini, and A. Vulpiani (1997), Dispersion of passive tracers in closed basins: Beyond the diffusion coefficient, *Phys. Fluids*, *9*(11), 3162-3171, doi:10.1063/1.869433.

Babiano, A., C. Basdevant, P. Leroy, and R. Sadourny (1987), Single-particle dispersion, Lagrangian structure function and Lagrangian energy spectrum in two-dimensional incompressible turbulence, *J. Mar. Res.*, *45*(1), 107-131, doi:10.1357/002224087788400936.

Bauer, S., M. S. Swenson, and A. Griffa (2002), Eddy mean flow decomposition and eddy diffusivity estimates in the tropical Pacific Ocean: 2. Results, *J. Geophys. Res.*, *107*(C10), 31-54, doi:10.1029/2000JC000613.

Berloff, P. S., J. C. McWilliams, and A. Bracco (2002), Material transport in oceanic gyres. Part I: Phenomenology, *J. Phys. Oceanogr.*, *32*(3), 764-796, doi:10.1175/1520-0485(2002)032<0764:MTIOGP>2.0.CO;2.

Berti, S., F. A. D. Santos, G. Lacorata, and A. Vulpiani (2011), Lagrangian drifter dispersion in the southwestern Atlantic Ocean, *J. Phys. Oceanogr.*, *41*(9), 1659-1672, doi:10.1175/2011JPO4541.1.

Boccaletti, G, R. Ferrari, and B. Fox-Kemper (2007), Mixed layer instabilities and restratification, *J. Phys. Oceanogr.*, *37*(9), 2228-2250, doi:10.1175/JPO3101.1.

Bracco, A., P. H. Chavanis, A. Provenzale, and E. A Spiegel (1999), Particle aggregation in a turbulent Keplerian flow. *Phys. Fluids*, *11*, 2280-2286, doi:10.1063/1.870090.

Bracco, A., J. H. LaCasce, and A. Provenzale (2000), Velocity probability density functions for oceanic floats. *J. Phys. Oceanogr., 30*, 461-474, doi:10.1175/1520-0485(2000)030<0461:VPDFFO>2.0.CO;2.

Bracco, A., E. P. Chassignet, Z. D. Garraffo, and A. Provenzale (2003), Lagrangian velocity distributions in a high-resolution numerical simulation of the North Atlantic. *J. Atmos. Ocean. Tech.*, *20*, 1212-1220, doi:10.1175/1520-0426(2003)020<1212:LVDIAH>2.0.CO;2.

Bracco, A., J. von Hardenberg, A. Provenzale, J. B. Weiss, and J. C. McWilliams (2004), Dispersion and mixing in quasigeostrophic turbulence, *Phys. Rev. Lett.*, *92*(8), 084501, doi:10.1103/PhysRevLett.92.084501.

Butler, J. N., B. F. Morris, J. Cadwallader, and A. W. Stoner (1983), Studies of Sargassum and the Sargassum community. Bermuda Biological Station Special Publication.

Capet, X., J. C. McWilliams, M. J. Molemaker, and A. F. Shchepetkin (2008a), Mesoscale to submesoscale transition in the California Current system. Part I: Flow structure, eddy flux, and observational tests, *J. Phys. Oceanogr.*, *38*(1), 29-43, doi:10.1175/2007JPO3671.1.

Capet, X., J. C. McWilliams, M. J. Molemaker, and A. F. Shchepetkin (2008b), Mesoscale to submesoscale transition in the California Current system. Part II: Frontal processes, *J. Phys. Oceanogr.*, *38*(1), 44-64, doi:10.1175/2007JPO3672.1.

Capet, X., J. C. McWilliams, M. J. Molemaker, and A. F. Shchepetkin (2008c), Mesoscale to submesoscale transition in the California Current system. Part III: Energy balance and flux, *J. Phys. Oceanogr.*, *38*(10), 2256-2269, doi:10.1175/2008jpo3810.1.

Cardona, Y., and A. Bracco (2012), Enhanced vertical mixing within mesoscale eddies due to high frequency winds in the South China Sea, *Ocean Model.*, *42*, 1-15, doi:10.1016/j.ocemod.2011.11.004.

Carton, J. A., and B. S. Giese (2008), A reanalysis of ocean climate using Simple Ocean Data Assimilation (SODA), *Mon. Weather Rev.*, *136*(8), 2999-3017, doi:10.1175/2007MWR1978.1.

Chin, T. M., R. F. Milliff, and W. G. Large (1998), Basin-scale, high-wavenumber sea surface wind fields from a multiresolution analysis of scatterometer data, *J. Atmos. Ocean. Tech.*, *15*(3), 741-763, 9doi:10.1175/1520-0426(1998)015<0741:BSHWSS>2.0.CO;2.

Conkright, M. E., R. A. Locarnini, H. E. Garcia, T. D. O'Brien, T. Boyer, C. Stephens and J. I. Antonov (2002), World Ocean Atlas 2001: Objective Analyses, Data Statistics, and Figures, CD-ROM Documentation. National Oceanic Data Center, Silver Spring, MD, 17pp.

Cooper, C., G. Z. Forristall, and T. M. Joyce (1990), Velocity and hydrographic structure of two Gulf of Mexico warm-core rings, *J. Geophys. Res.*, *95*(C2), 1663-1679, doi:10.1029/JC095iC02p01663.

Crisanti, A., M. Falcioni, A. Provenzale, P. Tanga, and A. Vulpiani (1992(, Dynamics of passively advected impurities in simple two-dimensional flow models. *Physics of Fluids A-Fluid, 4***,** 1805-1820, doi:10.1063/1.858402.

D'Asaro, E., C. Lee, L. Rainville, R. Harcourt, and L. Thomas (2011), Enhanced turbulence and energy dissipation at ocean fronts, *Science*, *332*(6027), 318-322, doi:10.1126/science.1201515.

Danioux, E., P. Klein, and P. Rivière (2008), Propagation of wind energy into the deep ocean through a fully turbulent mesoscale eddy field, *J. Phys. Oceanogr.*, *38*(10), 2224-2241, doi:10.1175/2008JPO3821.1.

Danioux, E., P. Klein, M. W. Hecht, N. Komori, G. Roullet, and S. Le Gentil (2011), Emergence of wind-driven near-inertial waves in the deep ocean triggered by small-scale eddy vorticity structures, *J. Phys. Oceanogr.*, *41*(7), 1297-1307, doi:10.1175/2011JPO4537.1.

de Verdiere, A. C. (1983), Lagrangian eddy statistics from surface drifters in the eastern North Atlantic, *J. Mar. Res.*, *41*(3), 375-398, doi:10.1357/002224083788519713.

Dietrich, J. C., et al. (2012), Surface trajectories of oil transport along the Northern Coastline of the Gulf of Mexico, *Cont. Shelf Res.*, *41*(0), 17-47, doi:10.1016/j.csr.2012.03.015.

Di Lorenzo, E., A. J. Miller, D. J. Neilson, B. D. Cornuelle, and J. R. Moisan (2004), Modelling observed California Current mesoscale eddies and the ecosystem response. *Int. J. Remote Sens., 25*, 1307-1312, doi:10.1080/01431160310001592229.

d'Ovidio, F., J. Isern-Fontanet, C. López, E. Hernández-García and E. García-Ladona (2009), Comparison between Eulerian diagnostics and finite-size Lyapunov exponents computed from altimetry in the Algerian Basin, *Deep Sea Res. I*, *56*(1), 15-31, doi:10.1016/j.dsr.2008.07.014.

Drake, P. T., C. A. Edwards, and J. A. Barth (2011), Dispersion and connectivity estimates along the U.S. west coast from a realistic numerical model, *J. Mar. Res.*, *69*(1), 1-37, doi:10.1357/002224011798147615.

Elhmaïdi, D., A. Provenzale, and A. Babiano (1993), Elementary topology of two-dimensional turbulence from a Lagrangian viewpoint and single-particle dispersion, *J. Fluid Mech.*, *257*, 533-558, doi: 10.1017/S0022112093003192.

Elliott, B. A. (1982), Anticyclonic rings in the Gulf of Mexico. *J. Phys. Oceanogr., 12*, 1292-1309, doi:10.1175/1520-0485(1982)012<1292:ARITGO>2.0.CO;2.

Falco, P., A. Griffa, P.-M. Poulain, and E. Zambianchi (2000), Transport properties in the Adriatic Sea as deduced from drifter data, *J. Phys. Oceanogr.*, *30*(8), 2055-2071, doi:10.1175/1520-0485(2000)030<2055:TPITAS>2.0.CO;2.

Faller, A. J., and A. H. Woodcock (1964), The spacing of windrows of Sargassum in the ocean. *J. Mar. Res., 22*, 22-29.

Ferrari, R., and D. L. Rudnick (2000), Thermohaline variability in the upper ocean, *J. Geophys. Res., 105*, 16857-16883.

Forristall, G. Z., K. J. Schaudt, and C. K. Cooper (1992), Evolution and kinematics of a loop current eddy in the Gulf of Mexico during 1985, *J. Geophys. Res*, *97*(C2), 2173-2184, doi:10.1029/91JC02905.

Fox-Kemper, B., R. Ferrari, and R. Hallberg (2008), Parameterization of mixed layer eddies. Part I: Theory and diagnosis, *J. Phys. Oceanogr.*, *38*(6), 1145-1165, doi:10.1175/2007JPO3792.1.

Gildor, H., E. Fredj, J. Steinbuck, and S. Monismith (2009), Evidence for submesoscale barriers to horizontal mixing in the ocean from current measurements and aerial photographs, *J. Phys. Oceanogr.*, *39*(8), 1975-1983, doi:10.1175/2009JPO4116.1.

Gower, J., and S. King (2008), Satellite images show the movement of floating *Sargassum* in the Gulf of Mexico and Atlantic Ocean, *Nature Precedings*, hdl:10101/npre.2008.1894.1.

Gower, J. F. R., and S. A. King (2011), Distribution of floating Sargassum in the Gulf of Mexico and the Atlantic Ocean mapped using MERIS. *Int. J. Remote Sens., 32*, 1917-1929, doi: 10.1080/01431161003639660.

Graves, L. P., J. C. McWilliams, and M. T. Montgomery (2006), Vortex evolution due to straining: a mechanism for dominance of strong, interior anticyclones. *Geophys. Astro. Fluid, 100*, 151-183, doi:10.1080/03091920600792041.

Haza, A. C., T. M. Özgökmen, A. Griffa, Z. D. Garraffo, and L. Piterbarg (2012), Parameterization of particle transport at submesoscales in the Gulf Stream region using Lagrangian subgridscale models, *Ocean Model.*, *42*, 31-49, doi:10.1016/j.ocemod.2011.11.005.

Jouanno, J., J. Sheinbaum, B. Barnier, J. M. Molines, L. Debreu, and F. Lemarié (2008), The mesoscale variability in the Caribbean Sea. Part I: Simulations and characteristics with an embedded model. *Ocean Model., 23*, 82-101, doi:10.1016/j.ocemod.2008.04.002.

Kalnay, E., M. Kanamitsu, R. Kistler, W. Collins, D. Deaven, L. Gandin, M. Iredell, S. Saha, G. White, J. Woollen, Y. Zhu, M. Chelliah, W. Ebisuzaki, W. Higgins, J. Janowiak, K. C. Mo, C. Ropelewski, J. Wang, A. Leetmaa, R. Reynolds, R. Jenne, and D. Joseph (1996), The NCEP/NCAR 40-year reanalysis project, Bulletin of the (1996), The NCEP/NCAR 40-year reanalysis project, *Bull. Amer.*

Meteor. Soc., *77*(3), 437-471, doi:10.1175/1520-0477(1996)077<0437:TNYRP>2.0.CO;2.

Kantha, L. H., and C. A. Clayson (2000), *Numerical Models of Oceans and Oceanic Processes*, Vol. 66 (International Geophysics), Acedemic Press, pp. 750.

Keating, S. R., K. S. Smith, and P. R. Kramer (2011), Diagnosing lateral mixing in the upper ocean with virtual tracers: spatial and temporal resolution dependence, *J. Phys. Oceanogr.*, *41*(8), 1512-1534, doi:10.1175/2011JPO4580.1.

Kimura, Y., and J. R. Herring (1996), Diffusion in stably stratified turbulence, *J. Fluid Mech.*, *328*, 253-269, doi:10.1017/S0022112096008713.

Klein, P., and G. Lapeyre (2009), The oceanic vertical pump induced by mesoscale and submesoscale turbulence, *Ann. Rev. Mar. Science*, *1*(1), 351-375, doi:10.1146/annurev.marine.010908.163704.

Klein, P., A.-M. Tréguier and B. L. Hua (1998), Three-dimensional stirring of thermohaline fronts, *J. Mar. Res.*, *56*(3), 589-612, doi:10.1357/002224098765213595.

Klein, P., G. Lapeyre, and W. G. Large (2004), Wind ringing of the ocean in presence of mesoscale eddies, *Geophys. Res. Lett.*, *31*(15), L15306, doi:10.1029/2004GL020274.

Klein, P., B. L. Hua, G. Lapeyre, X. Capet, S. Le Gentil, and H. Sasaki (2008), Upper ocean turbulence from high-resolution 3D simulations, *J. Phys. Oceanogr.*, *38*(8), 1748-1763, doi:10.1175/2007JPO3773.1.

Koszalka, I., A. Bracco, J. C. McWilliams, and A. Provenzale (2009), Dynamics of wind-forced coherent anticyclones in the open ocean, *J. Geophys. Res.*, *114*(C8), C08011, doi:10.1029/2009jc005388.

Koszalka, I., L. Ceballos, and A. Bracco (2010), Vertical mixing and coherent anticyclones in the ocean: The role of stratification, *Nonlin. Processes Geophys.*, *17*(1), 37-47, doi:10.5194/npg-17-37-2010.

Kunze, E. (1985), Near-inertial wave propagation in geostrophic shear, *J. Phys. Oceanogr.*, *15*(5), 544-565, doi:10.1175/1520-0485(1985)015<0544:NIWPIG>2.0.CO;2.

LaCasce, J. H. (2008), Statistics from Lagrangian observations, *Prog. Oceanogr.*, *77*(1), 1-29, doi:10.1016/j.pocean.2008.02.002.

Langmuir, I. (1938), Surface motion of water induced by wind. *Science, 87*, 119-123, doi:10.1126/science.87.2250.119.

Large, W. G., J. C. McWilliams, and S. C. Doney (1994), Oceanic vertical mixing: A review and a model with a nonlocal boundary layer parameterization. *Rev. Geophys., 32*, 363-403, doi:10.1029/94rg01872.

Ledwell, J. R., E. T. Montgomery, K. L. Polzin, L. C. St. Laurent, R. W. Schmitt, and J. M. Toole (2000), Evidence for enhanced mixing over rough topography in the abyssal ocean, *Nature*, *403*(6766), 179-182, doi:10.1038/35003164.

Le Traon, P. Y., P. Klein, B. L. Hua, and G. Dibarboure (2008), Do altimeter wavenumber spectra agree with the interior or surface quasigeostrophic theory?, *J. Phys. Oceanogr.*, *38*, 1137-1142, doi:10.1175/2007JPO3806.1

Lévy, M., P. Klein, A.-M. Tréguier, D. Iovino, G. Madec, S. Masson, and K. Takahashi (2010), Modifications of gyre circulation by sub-mesoscale physics, *Ocean Model.*, *34*, 1-15, doi:10.1016/j.ocemod.2010.04.001.

Lévy, M., R. Ferrari, P. J. S. Franks, A. P. Martin, and P. Rivière (2012), Bringing physics to life at the submesoscale, *Geophys. Res. Lett.*, *39*(14), L14602, doi:10.1029/2012GL052756.

Li, Q. P., P. J. S. Franks, M. D. Ohman, and M. R. Landry (2012), Enhanced nitrate fluxes and biological processes at a frontal zone in the southern California current system, *J. Plankton Res.*, *34*(9), 790-801, doi:10.1093/plankt/fbs006.

Lumpkin, R., A.-M. Treguier, and K. Speer (2002), Lagrangian eddy scales in the northern Atlantic ocean. *J. Phys. Oceanogr., 32*, 2425-2440, doi: 10.1175/1520-0485(2002)032<2425:lesitn>2.0.co;2.

Luo, H., A. Bracco, and E. Di Lorenzo (2011), The interannual variability of the surface eddykinetic energy in the Labrador Sea. *Prog. Oceanogr., 91*, 295-311, doi:10.1016/j.pocean.2011.01.006.

Mahadevan, A. (2006), Modeling vertical motion at ocean fronts: Are nonhydrostatic effects relevant at submesoscales?, *Ocean Model.*, *14*(3-4), 222-240, doi:10.1016/j.ocemod.2006.05.005.

Mahadevan, A., and A. Tandon (2006), An analysis of mechanisms for submesoscale vertical motion at ocean fronts, *Ocean Model.*, *14*(3-4), 241-256, doi:10.1016/j.ocemod.2006.05.006.

Mahadevan, A., L. N. Thomas, and A. Tandon (2008), Comment on "Eddy/wind interactions stimulate extraordinary Mid-ocean plankton blooms". *Science, 320*, 448, doi:10.1126/science.1152111.

Mahadevan, A., A. Tandon, and R. Ferrari (2010), Rapid changes in mixed layer stratification driven by submesoscale instabilities and winds, *J. Geophys. Res.*, *115*(C3), C03017, doi:10.1029/2008JC005203.

Mariano, A. J., V. H. Kourafalou, A. Srinivasan, H. Kang, G. R. Halliwell, E. H. Ryan, and M. Roffer (2011), On the modeling of the 2010 Gulf of Mexico Oil Spill, *Dyn. Atmos. Oceans*, *52*(1–2), 322-340, doi:10.1016/j.dynatmoce.2011.06.001.

Martin, A. P., and K. J. Richards (2001), Mechanisms for vertical nutrient transport within a North Atlantic mesoscale eddy, *Deep Sea Res. II*, *48*(4–5), 757-773, doi:10.1016/S0967-0645(00)00096-5.

Mason, E., J. Molemaker, A. F. Shchepetkin, F. Colas, J. C. McWilliams, and P. Sangrà (2010), Procedures for offline grid nesting in regional ocean models, *Ocean Model.*, *35*(1-2), 1-15, doi:10.1016/j.ocemod.2010.05.007.

Maxey, M. R., and J. J. Riley (1983), Equation of motion for a small rigid sphere in a nonuniform flow. *Phys. Fluids, 26*, 883-889, doi: 10.1063/1.864230.

McDonagh, E. L., and K. J. Heywood (1999), The Origin of an Anomalous Ring in the Southeast Atlantic. *J. Phys. Oceanogr., 29*, 2050-2064, doi:10.1175/1520-0485(1999)029<2050:TOOAAR>2.0.CO;2.

McWilliams, J. C. (1990), The vortices of two-dimensional turbulence. *J. Fluid Mech., 219*, 361-385, doi:10.1017/S0022112090002981.

McWilliams, J. C., L. P. Graves, and M. T. Montgomery (2003), A formal theory for vortex Rossby waves and vortex evolution. *Geophys. Astro. Fluid, 97*, 275-309, doi: 10.1080/0309192031000108698.

McWilliams, J. C., F. Colas, and M. J. Molemaker (2009a), Cold filamentary intensification and oceanic surface convergence lines, *Geophys. Res. Lett.*, *36*(18), L18602, doi:10.1029/2009GL039402.

McWilliams, J. C., M. J. Molemaker, and E. I. Olafsdottir (2009b), Linear fluctiation growth during frontogenesis. *J. Phys. Oceanogr., 39*, 3111-3129, doi: 10.1175/2009JPO4186.1.

Milliff, R. F., J. Morzel, D. B. Chelton, and M. H. Freilich (2004), Wind stress curl and wind stress divergence biases from rain effects on QSCAT surface wind retrievals, *J. Atmos. Oceanic Technol.*, *21*(8), 1216-1231, doi:10.1175/1520-0426(2004)021<1216:WSCAWS>2.0.CO;2.

Molemaker, M. J., J. C. McWilliams, and I. Yavneh (2005), Baroclinic instability and loss of balance, *J. Phys. Oceanogr.*, *35*(9), 1505-1517, doi: 10.1175/JPO2770.1.

Molemaker, M. J., J. C. McWilliams, and X. Capet (2010), Balanced and unbalanced routes to dissipation in an equilibrated Eady flow, *J. Fluid Mech.*, *654*, 35-63, doi:10.1017/S0022112009993272.

Montgomery, M. T., and R. J. Kallenbach (1997), A theory for vortex Rossby-waves and its application to spiral bands and intensity changes in hurricanes. *Q. J. Roy. Meteorol. Soc., 123*, 435-465, doi:10.1002/qj.49712353810.

Nagai, T., A. Tandon, D. L. Rudnick (2006), Two-dimensional ageostrophic secondary circulation at ocean fronts due to vertical mixing and large-scale deformation, *J. Geophys. Res.*, *100*, C09038, doi:10.1029/2005JC002964.

North, E. W., E. E. Adams, Z. Schlag, C. R. Sherwood, R. He, K. H. Hyun, and S. A. Socolofsky (2011), Simulating Oil Droplet Dispersal From the *Deepwater Horizon* Spill With a Lagrangian Approach, in *Monitoring and Modeling the Deepwater Horizon Oil Spill: A Record-Breaking Enterprise*, *Geophys. Monogr. Ser.* vol. 195*,* edited by Y. Liu et al., pp. 217-226, AGU, Washington, D. C, doi:10.1029/2011GM001102.

Oey, L.-Y, M. Inoue, R. Lai, X.-H. Lin, S. E. Welsh, and L. J. Rouse Jr. (2008), Stalling of near-inertial waves in a cyclone, *Geophys. Res. Lett.*, *35*, L12604, doi:10.1029/2008GL034273

Ohlmann, J. C., and S. Mitarai (2010), Lagrangian assessment of simulated surface current dispersion in the coastal ocean, *Geophys. Res. Lett.*, *37*, L17602, doi:10.1029/2010GL044436.

Okubo, A. (1970), Horizontal dispersion of floatable particles in the vicinity of velocity singularities such as convergences. *Deep Sea Research and Oceanographic Abstracts, 17*, 445-454, doi: 10.1016/0011-7471(70)90059-8.

Osborne, A. R., A. D. Kirwan, A. Provenzale, and L. Bergamasco (1989), Fractal drifter trajectories in the Kuroshio extension, *Tellus A*, *41A*(5), 416-435, doi:10.1111/j.1600-0870.1989.tb00392.x.

Paillet, J. (1999), Central water vortices of the eastern North Atlantic. *J. Phys. Oceanogr., 29*, 2487-2503, doi:10.1175/1520-0485(1999)029<2487:CWVOTE>2.0.CO;2.

Pasquero, C., A. Provenzale, and A. Babiano (2001), Parameterization of dispersion in two-dimensional turbulence, *J. Fluid Mech.*, *439*, 279-303, doi:10.1017/S0022112001004499.

Pinot, J.-M., J. Tintoré, and D.-P. Wang (1996), A study of the omega equation for diagnosing vertical motions at ocean fronts, *J. Mar. Res.*, *54*(2), 239-259, doi:10.1357/0022240963213358.

Poje, A. C., A. C. Haza, T. M. Özgökmen, M. G. Magaldi, and Z. D, Garraffo (2010), Resolution dependent relative dispersion statistics in a hierarchy of ocean models, *Ocean Model.*, *31*, 36-50, doi:10.1016/j.ocemod.2009.09.002.

Polzin, K. L., J. M. Toole, J. R. Ledwell, and R. W. Schmitt (1997), Spatial variability of turbulent mixing in the abyssal ocean, *Science*, *276*(5309), 93-96, doi:10.1126/science.276.5309.93.

Provenzale, A. (1999), Transport by coherent barotropic vortices, *Annu. Rev. Fluid Mech.*, *31*, 55-93, doi:10.1146/annurev.fluid.31.1.55.

Reynolds, A. M. (2002), Lagrangian stochastic modeling of anomalous diffusion in two-dimensional turbulence. *Phys. Fluids, 14*, 1442-1449, doi:10.1063/1.1456063.

Richardson, P. L. (1993), A census of eddies observed in North Atlantic SOFAR float data. *Prog. Oceanogr., 31*, 1-50, doi: 10.1016/0079-6611(93)90022-6.

Rivas, D., A. Badan, J. Sheinbaum, J. Ochoa, and J. Candela (2008), Vertical velocity and vertical heat flux observed within Loop Current eddies in the central Gulf of Mexico, *J. Phys. Oceanogr.*, *38*(11), 2461-2481, doi:10.1175/2008JPO3755.1.

Rooker, J. R., S. A. Holt, R. D. Wells, J. P. Turner, and C. Pratt (2004), Retrospective determination of trophic relationships among pelagic fishes associated with Sargassum mats in the Gulf of Mexico. *Proceeding of the Gulf and Caribbean Fisheries Institute, 55*, 257-266.

Rupolo, V., B. L. Hua, A. Provenzale, and V. Artale (1996), Lagrangian velocity spectra at 700 m in the western North Atlantic, *J. Phys. Oceanogr.*, *26*(8), 1591-1607, doi:10.1175/1520-0485(1996)026<1591:LVSAMI>2.0.CO;2.

Sanderson, B. G., and D. A. Booth (1991), The fractal dimension of drifter trajectories and estimates of horizontal eddy-diffusivity, *Tellus A*, *43*(5), 334-349, doi:10.1034/j.1600-0870.1991.t01-1-00008.x.

Sarangi, R. K., P. Chauhan, and S. R. Nayak (2004), Detection and monitoring of Trichodesmium blooms in the coastal waters off Saurashtra coast, India using IRS-P4 OCM data. *Curr. Sci. India, 86*, 1636-1641.

Schroeder, K., J. Chiggiato, A. C. Haza, A. Griffa, T. M. Özgökmen, P. Zanasca, A. Molcard, M. Borghini, P. M. Poulain, R. Gerin, E. Zambianchi, P. Falco, and C. Trees (2012), Targeted Lagrangian sampling of submesoscale dispersion at a coastal frontal zone, *Geophys. Res. Lett.*, *39*(11), L11608, doi:10.1029/2012GL051879.

Schroeder, K., A. C. Haza, A. Griffa, T. M. Özgökmen, P. M. Poulain, R. Gerin, G. Peggion, and M. Rixen (2011), Relative dispersion in the Liguro-Provençal basin:

From sub-mesoscale to mesoscale, *Deep Sea Res. I*, *58*(3), 209-228, doi:10.1016/j.dsr.2010.11.004.

Scotti, A., and J. Pineda (2004), Observation of very large and steep internal waves of elevation near the Massachusetts coast, *Geophys. Res. Lett.*, *31*(22), L22307, doi:10.1029/2004GL021052.

Shay, L. K., A. J. Mariano, S. D. Jacob, and E. H. Ryan (1998), Mean and near-inertial ocean current response to Hurricane Gilbert, *J. Phys. Oceanogr., 28,* 858–889.

Shchepetkin, A. F., and J. C. McWilliams (2003), A method for computing horizontal pressure-gradient force in an oceanic model with a nonaligned vertical coordinate. *J. Geophys. Res.-Oceans, 108*, 3090, doi:10.1029/2001jc001047.

Shchepetkin, A. F., and J. C. McWilliams (2005), The regional oceanic modeling system (ROMS): A split-explicit, free-surface, topography-following-coordinate oceanic model, *Ocean Model.*, *9*(4), 347-404, doi:10.1016/j.ocemod.2004.08.002.

Shoosmith, D. R., P. L. Richardson, A. S. Bower, and H. T. Rossby (2005), Discrete eddies in the northern North Atlantic as observed by looping RAFOS floats. *Deep-Sea Res. PT II, 52*, 627-650, doi:10.1016/j.dsr2.2004.12.011.

Siegel, D. A., B. P. Kinlan, B. Gaylord, and S. D. Gaines (2003), Lagrangian descriptions of marine larval dispersion, *Mar. Ecol. Progr. Ser.*, *260*, 83-96, doi:10.3354/meps260083.

Smith, S. K., and R. Ferrari (2009), The Production and Dissipation of Compensated Thermohaline Variance by Mesoscale Stirring, *J. Phys. Oceanogr.*, *39*(10), 2477-2501, doi:10.1175/2009JPO4103.1.

Sturges, W., and K. E. Kenyon (2008), Mean flow in the Gulf of Mexico, *J. Phys. Oceanogr.*, *38*(7), 1501-1514, doi:10.1175/2007jpo3802.1.

Subramaniam, A., C. W. Brown, R. R. Hood, E. J. Carpenter, and D. G. Capone (2002), Detecting Trichodesmium blooms in SeaWiFS imagery. *Deep-Sea Res. PT II, 49*, 107-121, doi:10.1016/s0967-0645(01)00096-0.

Sundelöf, A., and P. R. Jonsson (2012), Larval dispersal and vertical migration behaviour – a simulation study for short dispersal times, *Mar. Ecol.*, *33*(2), 183-193, doi:10.1111/j.1439-0485.2011.00485.x.

Tanga, P., and A. Provenzale (1994), Dynamics of advected tracers with varying buoyance. *Physica D, 76*, 202-215, doi: 10.1016/0167-2789(94)90259-3.

Taylor, G. I. (1921), Diffusion by continuous movements, *Proc. London Math. Soc.*, *s2-20*(1), 196-212, doi:10.1112/plms/s2-20.1.196.

Tél, T., G. Károlyi, Á. Péntek, I. Scheuring, Z. Toroczkai, C. Grebogi, and J. Kadtke (2000), Chaotic advection, diffusion, and reactions in open flows, *Chaos, 10*(1), 89-98, doi: 10.1063/1.166478.

Thomas, L. N., and R. Ferrari (2008), Friction, frontogenesis, and the stratification of the surface mixed layer, *J. Phys. Oceanogr.*, *38*(11), 2501-2518, doi:10.1175/2008JPO3797.1.

Thomas, L. N., A. Tandon, and A. Mahadevan (2008), Submesoscale processes and dynamics, in *Ocean Modeling in an Eddying Regime, Geophys. Monogr. Ser.*, vol. 177, edited by M. W. Hecht and H. Hasumi, pp. 17-38, AGU, Washington, D. C., doi:10.1029/177GM04.

Toole, J. M., R. W. Schmitt, and K. L. Polzin (1994), Estimates of diapycnal mixing in the abyssal ocean, *Science*, *264*(5162), 1120-1123, doi:10.1126/science.264.5162.1120.

Ullman, D. S., and P. C. Cornillon (1999), Satellite-derived sea surface temperature fronts on the continental shelf off the northeast U.S. coast. *J. Geophys. Res., 104*, 23459-23478, doi:10.1029/1999jc900133.

van Aartrijk, M., and H. J. H. Clercx (2010), Vertical dispersion of light inertial particles in stably stratified turbulence: The influence of the Basset force, *Phys. Fluids*, *22*(1), 013301, doi:10.1063/1.3291678.

van Aartrijk, M., H. J. H. Clercx, and K. B. Winters (2008), Single-particle, particle-pair, and multiparticle dispersion of fluid particles in forced stably stratified turbulence, *Phys. Fluids*, *20*(2), 025104, doi:10.1063/1.2838593.

van Haren, H., C. Millot, and I. Taupier-Letage (2006), Fast deep sinking in Mediterranean eddies, *Geophys. Res. Lett.*, *33*(4), L04606, doi:10.1029/2005GL025367.

Vitousek, S., and O. B. Fringer (2011), Physical vs. numerical dispersion in nonhydrostatic ocean modeling, *Ocean Model.*, *40*(1), 72-86, doi:10.1016/j.ocemod.2011.07.002.

Vukovich, F. M., and B. W. Crissman (1986), Aspects of warm rings in the Gulf of Mexico. *J. Geophys. Res.-Oceans, 91*, 2645-2660, doi:10.1029/JC091iC02p02645.

Vukovich, F. M. (1995), An updated evaluation of the Loop Current's eddy-shedding frequency, *J. Geophys. Res.*, *100*(C5), 8655-8659, doi:10.1029/95jc00141.

Weiss, J. (1991), The dynamics of enstrophy transfer in two-dimensional hydrodynamics. *Physica D, 48*, 273-294, doi:10.1016/0167-2789(91)90088-Q.

Winge, O. (1923), The Sargasso Sea, its boundaries and vegetation. *Report of the Danish Oceanographic Expedition, 3*, 1908-1910.

Zhong, Y., A. Bracco, and T. A. Villareal (2012), Pattern formation at the ocean surface: *Sargassum* distribution and the role of the eddy field, *Limn. Oceanogr.: Fluids & Envir.*, *2*, 12-27, doi:10.1215/21573689-1573372.

Zhong, Y. and A. Bracco (2013), Submeoscale impacts on horizontal and vertical transport in the Gulf of Mexico, *J. Geophys. Res.*, *118*, 1-18, doi:10.1002/jgrc.20402.